

Thermal Properties of Structure I Hydrates Using Density Functional Theory

Samuel Mathews

Department of Chemical Engineering

McGill University, Montreal

April 2020

A thesis submitted to McGill University in partial fulfillment of the
requirements of the degree of Master of Engineering in Chemical
Engineering

Abstract

Under certain conditions, water and small gaseous molecules form solid, crystalline gas hydrates, members of a larger class of structures called inclusion compounds or clathrates. Gas hydrates have previously been examined in the petroleum industry due to their propensity to cause flow assurance and safety issues and currently are examined as potential natural gas and hydrogen containers, as well as in separation processes to selectively capture flue gases. Thermal properties research has been centered around heat capacity and thermal expansion coefficient, experientially and theoretically. By using the Vienna ab initio Simulation Package (VASP) to solve the Schrödinger Equation in the context of Density Functional Theory, this research brought the gap between simulation and experiment by calculating the thermal properties of sI gas hydrates, using Phonopy paired with VASP, and to provide nanoscale insight into macroscale behavior.

The constant volume heat capacity, the constant pressure heat capacity, the volumetric thermal expansion coefficient, and the Grüneisen parameter of methane, ethane, carbon dioxide, and empty sI hydrates, and of hexagonal ice, as functions of temperature from 0 to 300 Kelvin were calculated using DFT. The constant volume heat capacity was lower than when compared with literature values calculated with MD. DFT replicated experimental values of constant pressure heat capacity for hydrates and ice well at low temperatures. DFT underestimated the thermal expansion coefficient in all cases. The ethane and carbon dioxide hydrates demonstrated behavior that was markedly different when compared to methane and empty hydrates, and hexagonal ice. The Grüneisen parameter was calculated for all systems. DFT overestimated the value of the parameter for filled hydrates and hexagonal ice when compared to experimental hexagonal ice values.

Résumé

Dans certaines conditions, l'eau et les petites molécules gazeuses forment des hydrates de gaz solides et cristallins. Les hydrates de gaz ont déjà été examinés dans l'industrie pétrolière en raison de leur des problèmes d'assurance de débit et sont actuellement examinés en tant que conteneurs potentiels de gaz naturel et d'hydrogène, ainsi que dans les processus de séparation. La recherche sur les propriétés thermiques a été centrée sur la capacité thermique et le coefficient de dilatation thermique, expérimentalement et théoriquement. En utilisant le Vienna ab initio Simulation Package (VASP) pour faire des calculs de théorie de la densité fonctionnelle (DFT), cette recherche a permis de combler l'écart entre la simulation et l'expérience en calculant les propriétés thermiques des hydrates de gaz sI.

La capacité thermique à volume constant, la capacité thermique à pression constante, le coefficient de dilatation thermique volumétrique et le paramètre Grüneisen des hydrates de méthane, de l'éthane, du dioxyde de carbone et des hydrates sI vides, et de la glace hexagonale, en fonction de la température de 0 à 300 Kelvin ont été calculés. La capacité thermique à volume constant était inférieure à celle des valeurs de la littérature calculées avec la dynamique moléculaire (MD). DFT a reproduit les valeurs expérimentales de la capacité thermique à pression constante pour les hydrates et la glace bien à basse température. DFT a sous-estimé le coefficient de dilatation thermique dans tous les cas. Les hydrates d'éthane et de dioxyde de carbone ont démontré un comportement nettement différent par rapport au méthane et aux hydrates vides et à la glace hexagonale. Le paramètre Grüneisen a été calculé pour tous les systèmes. DFT a surestimé la valeur du paramètre pour les hydrates remplis et la glace hexagonale par rapport aux valeurs expérimentales de la glace hexagonale.

Acknowledgements

I would like to take this opportunity to thank the people around me who have made this research project a possibility and a great learning opportunity. I would like to express my immense gratitude towards Dr. Alejandro D. Rey and Dr. Phillip Servio. Their guidance, ideas, and devotion to this project have allowed me to thrive in this research environment. They allowed me to explore a project I was interested in. I would like to thank all the members of the HydrateTech Lab and the MMRG Lab, Oscar Matus Rivas, Sina Mirzaeirfard, Thomas Vlastic, Shaden Daghash, Ziheng Wang, Sayyed Ahmad Khadem, Jonathan Monahan, Philip Cimento, Adam McElligott, and Faraz Rajput, for allowing my experience to go beyond just being here for research.

I would also like to acknowledge the Natural Science and Engineering Research Council of Canada for the financial support and Compute Canada for computational resources and support.

Table of Contents

| | |
|---|------|
| Abstract..... | i |
| Résumé..... | ii |
| Acknowledgements..... | iii |
| Table of Contents..... | iv |
| List of Figures..... | vi |
| List of Tables..... | viii |
| 1 Introduction..... | 1 |
| 1.1 Introduction to Gas Hydrates..... | 1 |
| 1.2 Properties of Gas Hydrates..... | 5 |
| 1.3 Structure I Gas Hydrate..... | 7 |
| 1.4 Research Objectives..... | 8 |
| 2 Literature Review..... | 9 |
| 2.1 Structure I Gas Hydrate in Literature..... | 9 |
| 2.2 Density Functional Theory..... | 14 |
| 3 Methodology..... | 19 |
| 3.1 Exchange Correlation Functional Choice..... | 19 |
| 3.2 Structure Generation..... | 20 |
| 3.3 Preprocessing..... | 21 |

| | |
|---|----|
| 3.4 Force/Energy Calculation | 23 |
| 3.5 Postprocessing | 24 |
| 3.6 Computational Details | 26 |
| 4 Results and Discussion | 27 |
| 4.1 Constant Volume Heat Capacity..... | 27 |
| 4.2 Constant Pressure Heat Capacity | 29 |
| 4.3 Thermal Expansion Coefficient | 32 |
| 4.4 Grüneisen Parameter..... | 36 |
| 5 Conclusion | 39 |
| 6 References..... | 41 |

List of Figures

| | |
|---|----|
| Figure 1-1: Experimental Hydrate Regions in a Pressure-Temperature Diagram from [2] | 2 |
| Figure 1-2: Gas Hydrate Structures from [7]..... | 3 |
| Figure 1-3: Typical sI Gas Hydrate Showing Trapped Gas Molecules from [31]..... | 7 |
| Figure 1-4: Unit Cell of Hexagonal Ice from [32]..... | 8 |
| Figure 2-1: Methane and Ethane Hydrate Structural Transition from [34] | 9 |
| Figure 2-2: Temperature dependence of the thermal conductivity of combination gas hydrate (●), methane hydrate (○), and THF hydrate (×) This figure was reproduced from [53] | 12 |
| Figure 2-3: Heat Capacity of Molecular Dynamics (MD) Studies [54] Compared to Experimental (Exp.) Studies [55], [56] | 13 |
| Figure 4-1: Heat Capacity of sI Hydrates and Ice I _h Computed with DFT (solid lines) and MD [54] with Various Guest Molecules: EO (ethylene oxide), FA (formaldehyde), CP (cyclopentane), and Et (ethane)..... | 27 |
| Figure 4-2: Heat Capacity of sI Hydrates and Ice I _h Computed with DFT (solid lines), Experiment [55], [93] (points), and MD [54] (dashed lines) with Various Guest Molecules: EO (ethylene oxide), FA (formaldehyde), CP (cyclopentane), and Et (ethane), Me (methane), Pr (propane)... | 30 |
| Figure 4-3: Volumetric Thermal Expansion of sI Hydrates and Ice I _h Computed with DFT (thick solid lines), MD [54], [94] (dashed lines), and Experiment [95], [96] (solid lines)..... | 32 |

| | |
|--|----|
| Figure 4-4: Volumetric Thermal Expansion Coefficient of sI Hydrates and Ice I _h Computed With DFT | 34 |
| Figure 4-5: Methane Hydrate (top left), Empty Hydrate (top right), Carbon Dioxide Hydrate (bottom left), ethane hydrate (bottom right) Viewed Through the Hexagonal Face of the 5 ¹² 6 ² Cages, Generated with VESTA Visualization Software [98] | 35 |
| Figure 4-6: Grüneisen Parameter of sI Hydrates and Ice I _h Computed with DFT (solid lines) and Experimentally Determined for THF Hydrates and Ice I _h (points) [96] | 37 |

List of Tables

| | |
|--|----|
| Table 1: Elastic Constants of Gas Hydrates from Various Sources..... | 10 |
|--|----|

1 Introduction

1.1 Introduction to Gas Hydrates

Large scale gas hydrate research initiated as a broad program to analyze the economic feasibility of methane extraction from hydrates, which was undertaken by the United States Department of Energy. Various other governments undertook research after that, also aiming to study potential gas reserves [1]. Gas hydrates had previously been examined in the petroleum industry due to their propensity to cause flow assurance and safety issues [2]. Currently, hydrates are examined as potential natural gas and hydrogen containers, as well as in separation processes to selectively capture flue gases, such as carbon dioxide. Gas hydrates may also be used in desalination, as they can form in such a way that excludes salt ions [3]. Thanks to these advances, understanding the formation, dissociation, and properties of gas hydrates is becoming an increasingly important area of research to study both exploitation and their potential release associated with climate change [4].

Under certain conditions, water and small gaseous molecules form solid, crystalline gas hydrates. Hydrates are members of a larger class of structures called inclusion compounds or clathrates. In clathrates, a structure formed by molecules of one substance enclose a molecule of another substance. Hydrates are clathrates where the outer structure is formed by water molecules. Since the cage structure is formed by water molecules, hydrates are often compared to ice [2]. Water molecules interact via hydrogen bonds, which cause the molecules to align in a specific way, and the presence of another molecule affects the possible configurations of the structure. The guest molecule, in some cases, actually stabilizes the structure due to van der Waals forces [2], [5].

Low temperature and high-pressure favor hydrate formation. This means that it is possible to generate a temperature-pressure curve describing the hydrate conditions for a specific guest molecule, or former [2], as seen in Figure 1-1. The formation of specific gas hydrates is governed by pressure, temperature, and composition of the guest molecule [6].

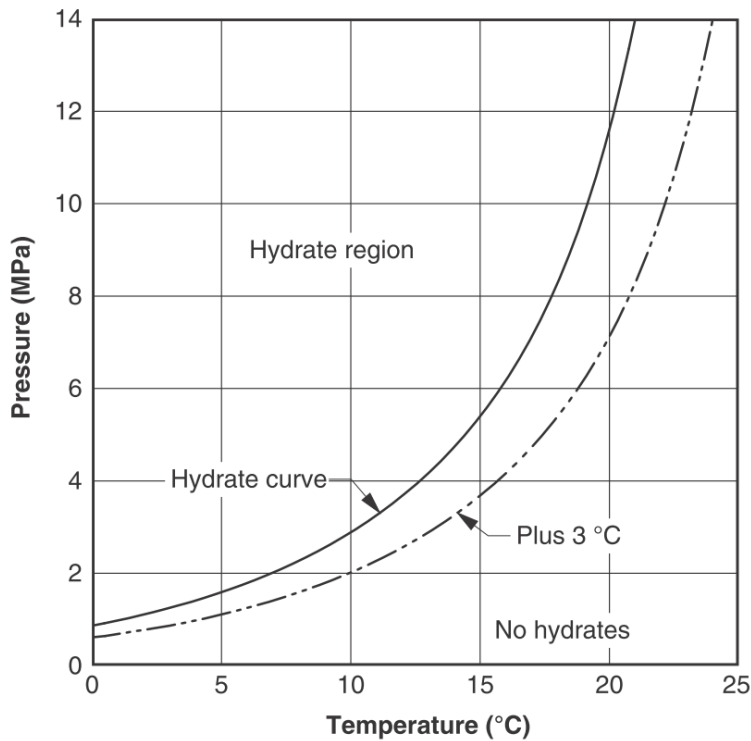


Figure 1-1: Experimental Hydrate Regions in a Pressure-Temperature Diagram from [2]

There exist three main structures of gas hydrates, structure I (sI), structure II (sII), and structure H (sH). Structure I hydrates are the simplest structure. They consist of 46 molecules arranged around the guest molecule in two different cage structures, a large and small cage. Formers of sI hydrates include carbon dioxide, methane, ethane, and hydrogen sulfide. Structure II hydrates consist of 136 water molecules that form larger and small cages. The occupancy of certain guest molecules is more complex than for sI hydrates due to the different size and structure of the hydrate. Structure H hydrates consist of 34 water molecules structure into three different

cages. These hydrates always form with two guests, one small one for the small and medium cages, and a larger one for the large cages [2]. These structures are represented in Figure 1-2.

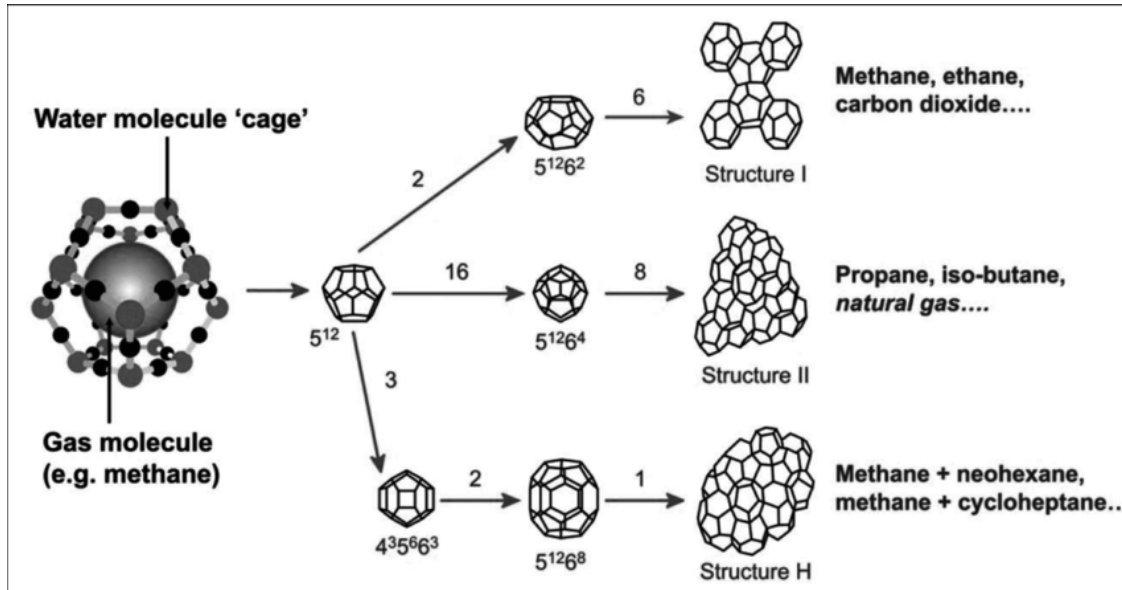


Figure 1-2: Gas Hydrate Structures from [7]

Determining the crystal structure of hydrates experimentally took a long time because hydrates are nonstoichiometric, meaning that a stable structure can form without 100% cage occupancy [2], [6], [8].

Gas hydrates are present around the world in various industries. In natural gas extraction, water is always present in natural gas reservoirs. Additionally, it is often used to remove carbon dioxide and hydrogen sulfide, “acid gases” present in the natural gas. Therefore, hydrates will be encountered throughout natural gas production [2], where they are considered a problem. Gas hydrates can also be used in gas separation, desalination, gas storage, and carbon dioxide sequestration due to their unique structural packing [9]–[11].

Techniques used to combat ice formation can also be used to combat hydrate formation. Polar solvents are commonly used to inhibit hydrate formation by increasing the pressure or reducing the temperature at which a hydrate will form. Ionic solids can also be used to inhibit hydrate formation. These inhibitors work by freezing point depression [2]. There exists another class of inhibitors, known as kinetic inhibitors, which work by delaying the onset of crystallization. However, crystallization will happen eventually, even in the presence of kinetic inhibitors [2], [12]. A third class of inhibitors, called anticoagulants, prevent the accumulation of hydrates which would lead to an eventual plug in a system that depends on the flow of a substance susceptible to hydrate formation. A final way to inhibit hydrate formation is to manipulate pressure and temperature conditions to ensure the operating point is always outside the hydrate formation zones [2].

Hydrate promoters exist to stimulate hydrate growth, which can be helpful in gas sequestration, for example. Certain surfactants exist to promote hydrate growth [13]. Some surfactants increase the rate of formation up to a certain point, while others do so for all concentrations [14]. Certain polymers have also shown to be hydrate promoters. They can do this kinetically and thermodynamically. Combining both may lead to even higher hydrate promotion [15].

Gas hydrates are also considered a large, global energy source. Enormous reserves are present under continental shelves across the world and the total amount of carbon in these reserves is estimated to nearly double the amount of carbon in all other fossil fuel reserves combined. Because cost, environmental concern, and resource availability all favor the use of natural gas, a common guest in hydrates, the exploitation of these reserves is becoming more important and necessary. To exploit them in a safe and effective manner, studying and predicting their properties

has become essential [6]. Various properties are exploited in various methods of natural gas hydrate exploitation, and these methods vary by location of the deposit [16], [17].

1.2 Properties of Gas Hydrates

Obtaining hydrate properties is often complicated because the properties depend on the cage occupancy, the guest molecule, and the structure of the hydrate [2]. For sI and sII gas hydrates, physical and chemical properties are well known, while sH is still lacking the same quality and quantity of data [18]. This arises because sH is not commonly seen in natural gas hydrate studies. However, it is becoming a structure of interest in other applications, such as gas storage [19], [20].

In general, the mechanical properties of gas hydrates are similar to those of ice, and often total equality is assumed because all three common structures encountered consist of approximately 85% water [6]. However, a first principles approach to modeling of hydrate systems yields more structure-specific and guest-specific data [2]. Using ice properties in place of hydrate properties is convenient but can introduce errors. For example, perfect ice crystals can be over than 1.5 times stronger than their sI perfect hydrate counterparts due to how the hydrate cavity nonuniformly deforms [5]. Thermal expansivity, yield strength, and thermal conductivity do not adhere to the ice-hydrate equality [6].

Hydrates and the sediments in which they are found have large variations in properties due to different hydrate and pore configurations. This leads to lower bulk densities than expected, when comparing theory and experiment. The bulk densities of the methane hydrates can vary between 0.35 and 0.75 kilograms per liter [21], with the variability a result of the different pore configurations in the sediment and different hydrate configurations and structures within the sediment.

Mechanical properties of gas hydrates vary with their structure. For example, the Zener anisotropy factor, a measure of how far the specific material is from being isotropic (where an A_z of 1 means it is isotropic), varies from 0.99 for a sI methane hydrate [5] to 1.13 for an ethane-methane sII gas hydrate [22]. In sII gas hydrates, the theoretical Young's modulus (E) can be 14.67 *GPa*, 11.57 *GPa*, or 12.58 *GPa*, depending on whether the lattice is empty, occupied by propane molecules, or occupied by a mixture of propane and methane molecules, respectively [22].

Thermal properties of gas hydrates are properties that poorly adhere to the ice-hydrate equality due to the addition of interactions with guest atoms which are not present in pure ice. While ice has a higher thermal conductivity than water, methane and propane gas hydrates have thermal conductivities about 30% lower than water [23]. Theoretically, the thermal expansion of ice I_h is $0.000125 K^{-1}$ while the methane hydrate has been measured to have a thermal expansion up to $0.000050 K^{-1}$ at certain conditions [24]. Due to difficulties in preparing and measuring properties of hydrates in the lab and comparing said properties to simulations, discrepancies in thermal properties exist even for the same hydrates. For example, the thermal conductivity of methane gas hydrates at 270 K has been measured to be 0.50, 0.57, 0.63, and 0.67 $W \cdot m^{-1} \cdot K^{-1}$ [25].

The vibrational properties of gas hydrates are becoming more important as tools to analyze samples of gas hydrates in the lab and in the field. For example, the Raman spectrum of hydrates can yield information regarding the structure, composition, and cage occupancy. There are marked differences between the Raman spectra of sI and sII methane hydrates [26]. Structure H hydrates have very little vibrational data available in literature because most research is centered around structure present in natural gas industries, sI and sII [27], [28]. The infrared spectrum of gas hydrates has been determined experimentally and from first principles for identification purposes, as well as to study the effect of promoters and inhibitors [29].

1.3 Structure I Gas Hydrate

In a unit cell, the structure I gas hydrate contains 46 water molecules and can accommodate eight guest molecules, as shown in Figure 1-3. Two pentagonal dodecahedral voids and six tetrakaidekahedron voids make up the arrangement. Structure I hydrates are made up of six large cages and two small cages and they crystallize in the $Pm\bar{3}n$ space group [30]. However, only small molecules can form sI gas hydrates. In terms of hydrocarbons, methane and ethane, but not propane, are known to be sI formers. Other small molecules, such as carbon dioxide, can also form sI gas hydrates [5], [6]. The unit cell of hexagonal ice is also shown for reference in Figure 1-4.

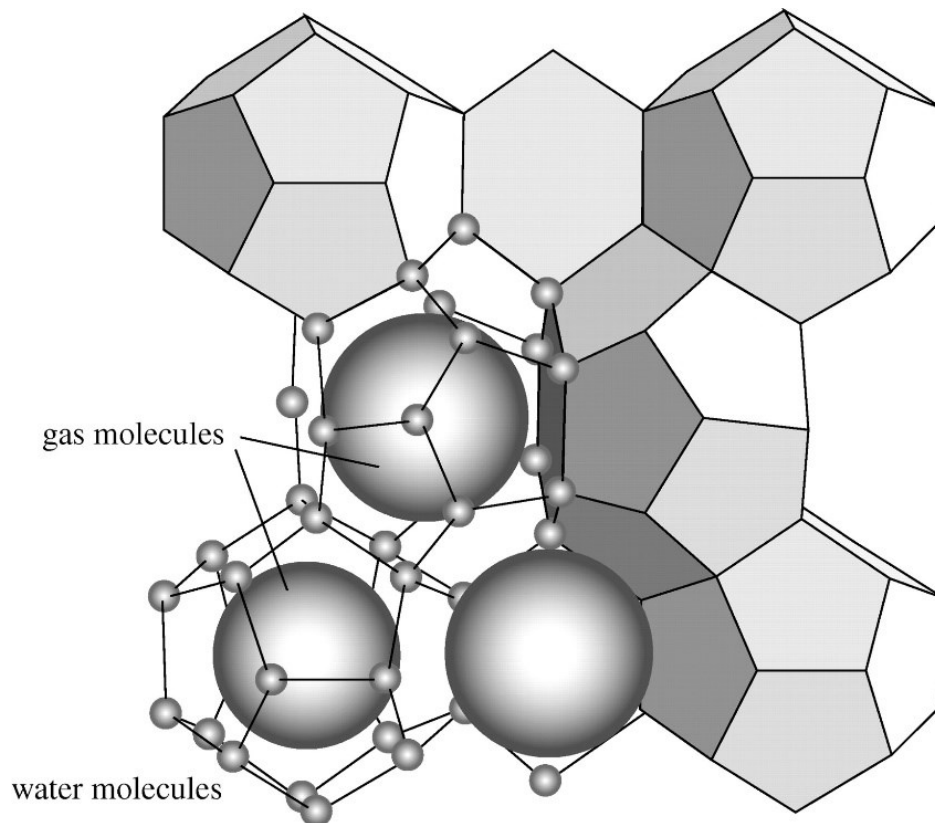


Figure 1-3: Typical sI Gas Hydrate Showing Trapped Gas Molecules from [31]

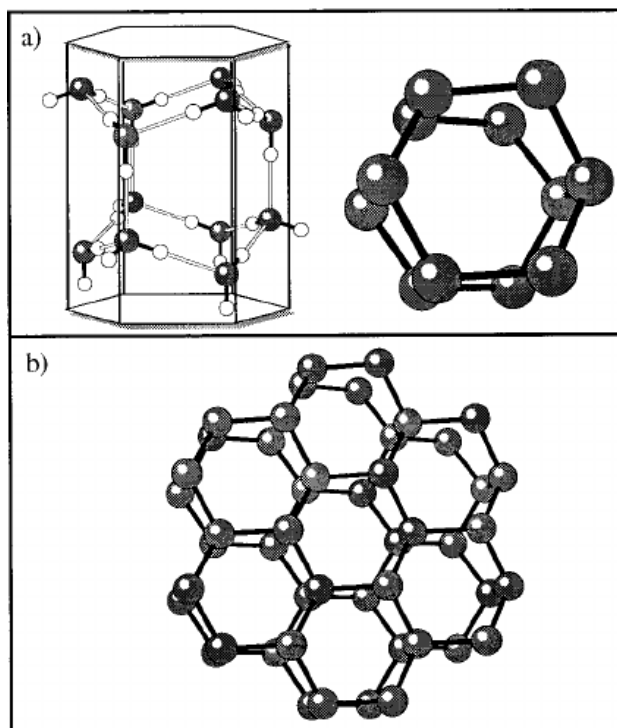


Figure 1-4: Unit Cell of Hexagonal Ice from [32]

1.4 Research Objectives

The main objective of this work is to calculate the constant volume heat capacity, the constant pressure heat capacity, the thermal expansion coefficient, and the Grüneisen Parameter of methane, ethane, carbon dioxide, and empty sI hydrates, and of hexagonal ice, as functions of temperature from 0 Kelvin to 300 Kelvin, to examine the similarities between the hydrate structures and ice, while providing insight into the influence of different guest molecules on the properties. As a part of this objective, this work sought to use computational techniques to use atomic-scale information, the atomic configurations, simulated in a zero-Kelvin environment, to explain and examine macroscopic, real-temperature behavior. This work sought to perform these calculations using *ab initio* density functional theory to remove the need for empirically determined parameters where possible.

2 Literature Review

2.1 Structure I Gas Hydrate in Literature

Phase equilibrium is the most studied area of gas hydrate science because hydrate formation is a physical, not chemical process [33]. As such, this mechanism is governed by pressure, temperature, and phase concentrations. Many studies focus on this aspect of gas hydrates due to their importance in petroleum engineering and the natural gas industry. The use of inhibitors and promoters also affects phase equilibrium. Gas hydrates are in equilibrium with liquid water and vapor phases. [34] generated phase diagrams for methane and ethane gas hydrates, showing how they transitioned from sI to sII hydrates. This is displayed in Figure 2-1.

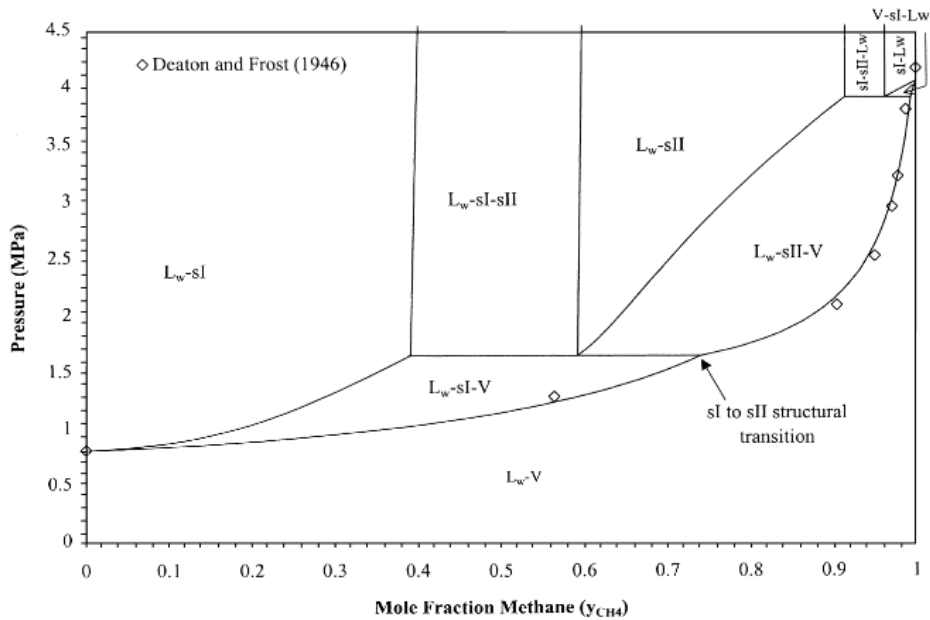


Figure 2-1: Methane and Ethane Hydrate Structural Transition from [34]

Another study [35] characterized the solubility of methane in hydrates to study its presence in deep sea sediments. The solubility was calculated for relevant pressures. At temperatures close

to lab or room temperatures, the driving forces are different than in the deep sea. For example, at 1.45, 6.49, and 12.91 °C, the overpressures required to trigger hydrate nucleation were 3, 5, and 10 MPa, respectively [36].

Various studies have examined the structural properties of gas hydrates, specifically the sI gas hydrate. Various experimental studies exist detailing structural properties [37]–[39], but due to the difficulty of producing pure hydrate samples in the lab, first-principles approaches are garnering interest [40]. These approaches allow for the simulation of guest molecules which may not be as common as methane in nature. For example, [5] used density functional theory to characterize the bulk modulus of the carbon dioxide hydrate and compared it to that of the sI methane hydrate. The carbon dioxide modulus is 3.98 GPa, while that of the methane hydrate is 9.82 GPa, yielding information on how different guest molecules contribute to strain. The same author calculated the bulk modulus of ice I_h at 7.81 GPa [41]. However, there are still discrepancies in calculated properties, as seen in Table 1, where different theoretical studies do not accurately describe any of the elastic constants determined experimentally.

Table 1: Elastic Constants of Gas Hydrates from Various Sources

| Study | c₁₁ (GPa) | c₁₂ (GPa) | C₄₄ (GPa) | A_z |
|-----------------------|-----------------------------|-----------------------------|-----------------------------|----------------------|
| Jendi et al. [5]* | 18.1 ± 0.2 | 5.7 ± 0.2 | 6.2 | 0.99 |
| Miranda et al. [42]* | 15.1 | 4.9 | 3.8 | 0.75 |
| Huo et al. [40]* | 14.2 | 6.0 | 7.9 | 1.90 |
| Shimizu et al. [43]** | 11.9 | 6.3 | 3.4 | 1.21 |

*Theoretical, 0K and 0 GPa **Experimental, 296K and 0.02 GPa •This table was reproduced from [5]

Thermodynamic properties of gas hydrates and methane/water systems are important because they elucidate details regarding stability, showing which conditions promote or inhibit hydrate formation. These properties are difficult or impossible to determine experimentally because the speed of crystallization makes it hard to examine the interfacial properties of the hydrate [44]. Therefore, molecular dynamics is often used to determine these properties. [45] studied the energy and surface tensions of a methane-water system near to and away from the hydrate formation threshold. The study found that the system is more stable at the hydrate formation threshold than away from it. It was also shown that at the threshold of hydrate formation, decreasing the temperature increases surface tensions, changing the formation conditions. This also showed that molecular dynamics simulations are in good agreement with experimental methods [46]–[50].

The thermal properties of gas hydrates are of interest in various industries and have been studied experimentally and theoretically. [51] separately developed temperature and pressure correlations for thermal conductivity, thermal diffusivity, and specific heat of methane hydrates. The purpose of the study was to determine these properties and compare them with hydrate-bearing sediment, determining other properties of importance in geology. Another study experimentally determined the heat capacity as a function of temperature for methane-krypton and methane-argon systems by comparing changes in dissociation pressure [52]. The thermal conductivity of combination gas (90.01 volume % methane, 5.03 volume % ethane, and 4.96 volume % propane) hydrates has also been studied and compared with pure sI methane hydrates and sII tetrahydrofuran hydrates [53]. Figure 2-2 presents some of the important findings of the study.

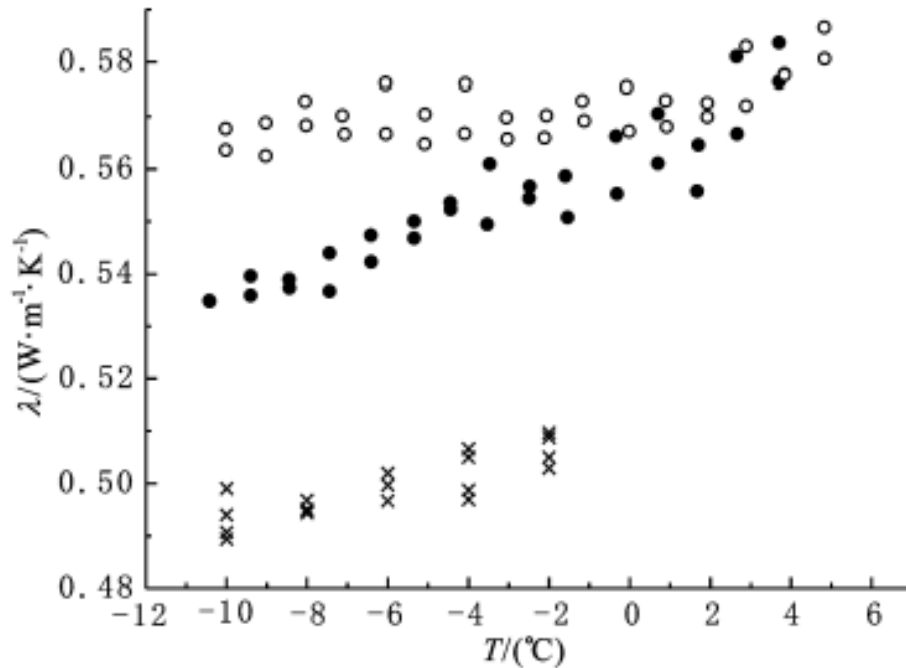


Figure 2-2: Temperature dependence of the thermal conductivity of combination gas hydrate (●), methane hydrate (○), and THF hydrate (×). This figure was reproduced from [53]

Figure 2-2 shows that the combination gas has a similar temperature dependence when compared to the THF hydrate but has the same thermal conductivity values when compared to the methane hydrate, at temperatures of -2 to 6 degrees Celsius. Further analysis showed that the combination gas formed an sII hydrate, meaning that thermal conductivity is both structure and guest correlative [53].

Theoretical methods, such as molecular dynamics, are now being used to investigate thermal properties. [23] calculated the thermal conductivity of a pure methane hydrate and compared it to experiment at various temperatures at 10 MPa. The results from the simulation were slightly higher than experiment, which was expected since experimental samples contain structural defects and residual porosity. Another study [25] found that the results for thermal

conductivity and other thermal properties varied with estimation techniques and the omission or inclusion of long-range electrostatics. Other molecular dynamics studies found some difference between guest molecules, but large differences with experiment, as show in Figure 2-3. The experimental studies showed very little difference between guest molecules, including between very polar and electron dense molecules compared to small, neutral molecules.

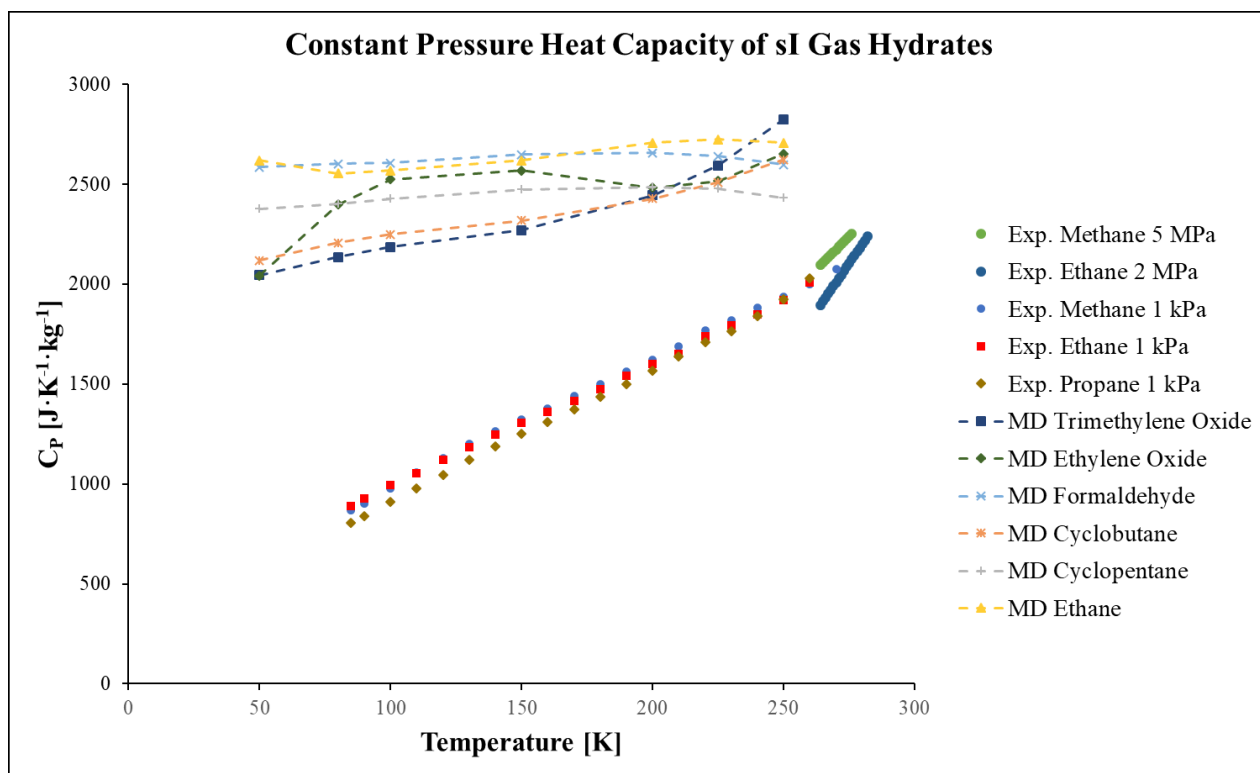


Figure 2-3: Heat Capacity of Molecular Dynamics (MD) Studies [54] Compared to Experimental (Exp.) Studies [55], [56]

First principles, theoretical approaches, such as density functional theory, are also used to determine thermal properties. [40] calculated the specific heat and thermal expansion coefficient of methane hydrates. When compared to experimental data, the specific heat of the sI hydrate was overestimated by 32.4% at $4369 \text{ J}\cdot\text{kg}^{-1}\cdot\text{K}^{-1}$. The specific heat of the sII hydrate was overestimated by 24.7% at $4488 \text{ J}\cdot\text{kg}^{-1}\cdot\text{K}^{-1}$. The authors theorized that this was partially due to the difference in

cage occupancy between the simulation (100%) and experiment (<100%). The thermal expansion coefficient for the sI hydrate was overestimated, and underestimated for the sII hydrate [40].

Another study [24] calculated the constant volume and pressure specific heats, as well the thermal expansion coefficient of the methane hydrate. The constant volume heat capacity was calculated with two equations, the derivative of the energy versus temperature at constant volume (Equation 2.1), and the fluctuation formula (Equation 2.2).

$$C_V = \left. \frac{\partial E}{\partial T} \right|_V \quad \text{Equation 2.1}$$

$$C_V = \frac{\langle E^2 \rangle - \langle E \rangle^2}{k_B T^2} \quad \text{Equation 2.2}$$

The results showed good agreement using both approaches in most cases and allowed the authors to produce a linear correlation for the constant volume heat capacity to be calculated as a function of time, with a coefficient of determination of 0.93. The calculated thermal expansion coefficient was almost 40% lower than another study [57] which calculated the same property, and higher than ice, which goes against what is commonly believed to be true. The constant pressure heat capacity was calculated and was more in agreement with another study [57] which also calculated the same property. The thermal expansion coefficient of both studies were within 7% of each other, and much closer to experimental data than thermal conductivity was [24].

2.2 Density Functional Theory

In the past ten years, computational power has increased by about 1000 times. This has allowed density functional theory to become a more accessible tool for high-end computational simulations. Density functional theory uses first principles methods based on the solution of

Schrödinger's equation. It breaks down the quantized interaction between particles into orbital equations. Solving these equations involves using exchange correlation functionals, which can provide accurate results in exchange for computational time and power. Once completed, the first principles calculations provide results without the need for empirical information, except for atomic positions which can be accurately determined via neutron scattering and x-ray diffraction [58].

Applying quantum mechanics to atoms helps identify fundamental properties of said atoms as zero Kelvin. A fundamental property of interest is the energy of the atoms and how this energy changes with atomic position. To tackle this calculation, the Born-Oppenheimer approximation is applied. This approximation allows the atom to be split into the nucleus and its electrons, since electrons are around 1800 times less massive than each proton or neutron. Electrons can therefore respond much faster to changes in atomic environment. Once the problem is divided, the ground state or lowest energy state of the electrons can be calculated [59].

To study the ground state energy of electrons and how this energy changes as the atoms are moved around, the time-independent, nonrelativistic, zero-Kelvin Schrödinger equation must be solved:

$$\left[-\frac{\hbar}{2m} \sum_{i=1}^N \nabla_i^2 + \sum_{i=1}^N V(\mathbf{r}_i) + \sum_{i=1}^N \sum_{j<i}^N U(\mathbf{r}_i, \mathbf{r}_j) \right] \psi = E\psi \quad \text{Equation 2.3}$$

In Equation 2.3, E is the ground state energy of the electrons, m is the electron mass, and ψ is the electronic wave function. The first term on the left is the kinetic energy of each electron, the second term is the interaction between each electron and the atomic nuclei, and the third term is the interaction between each electron. To simplify the Schrödinger equation, the Hartree product can

be used. Because the number of electrons is much larger than the number of nuclei. This product makes it possible to approximate Ψ as a product of each individual electron's wave function:

$$\Psi = \Psi_1 \Psi_2 \Psi_3 \dots \Psi_N \quad \text{Equation 2.4}$$

Using Equation 2.4 avoids complete wave functions of extremely high dimensions (due to the need to consider all interactions), which improves computational time. Due to quantum properties, the wave function cannot be directly observed. Therefore, a more useful quantity is the probability that electrons are in a certain place. This is called the electron density [59].

The electron density is more useful due to the first fundamental mathematical theorem of density functional theory. Proven by Kohn and Hohenberg, the theorem states: "*The ground-state energy from Schrödinger's equation is a unique functional of electron density*" [60]. This theorem has important ramifications. Instead of solving finding a complete wave function, a function of $3N$ variables (where N is the number of electrons), the Schrödinger equation can be solved by finding a function of three spatial variables, the electron density. This is because the energy and wave function of the ground state are uniquely determined by the ground-state electron density.

The second important theorem of density functional theory, also coming from the work of Kohn and Hohenberg, states: "*The electron density that minimizes the energy of the overall functional is the true electron density corresponding to the full solution of the Schrödinger equation*" [60]. By varying the electron density until the ground-state energy functional is minimized, a self-consistent solution to Schrödinger's equation can be found. The exact energy functional is not known, but the iterative process is still used on approximations of the functional [59].

To further simplify the problem, Kohn and Sham showed that the correct electron density can be found by solving sets of equations involving only one electron. This allowed for the calculation of single-electron wave functions from electron densities. The equations have the following form:

$$\left[-\frac{\hbar}{2m}\Delta^2 + V(\mathbf{r}) + V_H(\mathbf{r}) + V_{XC}(\mathbf{r}) \right] \psi_i(\mathbf{r}) = \varepsilon_i \psi_i(\mathbf{r}) \quad \text{Equation 2.5}$$

In Equation 2.5, the first term on the left describes the electron kinetic energies. The second term, V , describes the interaction between the electron and atomic nuclei. The third term, V_H , describes the Coulomb repulsion between all the electrons and the one in the current equation being considered. The fourth term, V_{XC} , describes the exchange correlation potential. This defines the quantum contributions of the electrons. The exchange correlation potential is the functional derivative of the exchange-correlation energy. When comparing Equation 2.3 to Equation 2.5, it is important to note the lack of summation signs in the latter. This results from the fact that the Kohn-Sham equations are single electron equations that depend on only three spatial dimensions, \mathbf{r} [59].

The iterative scheme used to calculate the ground state energy and electron density is as follows:

1. Define a trial electron density.
2. Solve the Kohn-Sham equations using the trial density to obtain the single-electron wave functions. The trial density appears in the calculation of the Hartree potential and exchange correlation potential in Equation 2.5.
3. Calculate the electron density resulting from the single-electron wave functions using the equation $n_{KS}(\mathbf{r}) = 2 \sum \psi_i^*(\mathbf{r})\psi_i(\mathbf{r})$, where the asterisk signals the complex conjugate of the wave function.

4. Compare the calculated and trial electron densities. If they are the same, the ground-state electron density is found. If they are different, the trial electron density is updated, and calculation started again from Step 2.

This iterative scheme governs density functional theory. Quantum calculators, such as the Vienna Ab Initio Simulation Package (VASP), use the same scheme with some optimizations, such as how to update the trial density, to improve computation times [59], [61].

3 Methodology

3.1 Exchange Correlation Functional Choice

The fourth term on the left side of Equation 2.5 is the exchange correlation potential, a function of the electron density. A large part of theoretical DFT research is currently focused on exchange correlation functionals, and because there is no systematic methodology, there exists a plethora of functionals to choose from. The chemical system determines the functional to be employed and the bonding environment differs from system to system, in most cases. The range of functionals goes from the lowest accuracy, the local density approximation, whose simplicity arose from lower computational power available, to very computationally expensive nonlocal functionals [62].

Meta-GGA (meta generalized gradient approximation) functionals are a recent development in this field and present a very appealing option. Specifically, the Strongly Constrained and Appropriately Normed Semilocal Density Functional (SCAN) provided the best option. The SCAN functional, at a minimum, duplicates the accuracy of more expensive hybrid functionals, which include some approximations and exact exchange, at a cost that is close to the generalized gradient approximation (GGA) functionals [63], [64]. Compared to other, older functionals, the SCAN functional provided the best error cancellation for atoms and Jellium Spheres [65].

An important complementary choice to the exchange correlation functional is how to account for long range dispersion interactions. For this work, a modified version of Vydrov-van Voorhis nonlocal correlation functional, called the rVV10 Functional of Peng et al. [66]–[69].

Using a nonlocal functional allows for the inclusion of long range exchange-correlation effects that appear because of electrons in remote areas of the atom's environment in the calculation that a semilocal functional alone could not take into account [62]. Therefore, the final exchange correlation functional used, as implemented in VASP, is the SCAN + rVV10 functional.

3.2 Structure Generation

When performing first principles calculations, it is important to have the ground state atomic configuration for the structure in question. This means generating atomic coordinates that correspond to the lowest energy state of the system, according to Equation 2.3. The first step of this process consisted of obtaining the atomic coordinates for the hydrate backbone unit cell, which provide a base for all other systems. The positions of the oxygen atoms were obtained from literature via X-ray diffraction, with the hydrogen atoms placed in a disordered fashion according to the Bernal-Fowler Ice Rules [70].

To generate the carbon dioxide, methane, and ethane hydrate structures, additional steps were required. [70] provides the atomic coordinates for the hydrate cage centers as well, which is where the guest molecules are located. For methane hydrates, the carbon atoms of the methane molecule were placed at the center of the cages. The protons were then placed around the carbon atom at the corresponding bond length and bond angles [71]. The molecule was oriented with the single proton pointing upward, but this was considered to be of negligible consequence because the methane molecule can rotate nearly freely in the cage according to experiment, and VASP will minimize the energy of the system by moving the ions, to a user determined tolerance, so if the molecules are not in the lowest energy state at this point, they will be moved to it mathematically, via the gradient of the energy [72].

The carbon dioxide and ethane hydrates followed a similar procedure to the methane hydrate. For carbon dioxide, the carbon atom was placed at the center of the cage and the oxygen atoms were placed in a linear fashion according to the bond lengths in literature [73]. For ethane, the midpoint between the carbon atoms was placed at the center of the cage, while their positions and those of the hydrogen atoms were placed according to bond lengths and angles in experiments [73]. Ethane and carbon dioxide are potentially large enough to not be able to rotate freely in the hydrate structure and their orientation may play a part in potential properties. However, VASP will perform structural optimization and will account for the role of orientation during minimization. The final structure to generate was hexagonal ice because it is often used to compare to hydrates and its properties are sometimes used instead of hydrate properties. The traditional Bernal-Fowler hexagonal ice lattice was used for this case. The coordinates of its unit cell were obtained from literature [74].

Once all the reference structures were obtained, they were relaxed via ionic relaxation by using VASP. VASP provides a variety of ionic minimization algorithms, but because the distance to the local minima is unknown, as is how much ionic movement will occur, the conjugate gradient algorithm was used, as opposed to the quasi-Newton algorithm, which performs better when the structure is close to a local minima but fails badly if the structure is far from it [75].

3.3 Preprocessing

Preprocessing involved generating the configuration files to be used in the Force/Energy calculation. Calculating the thermal properties of interest involved simulating thermal vibrations in the zero-Kelvin environment of DFT. Using the finite displacement method, as implemented in the open source package Phonopy, the properties were calculated by performing phonon

calculations [76]. Once the relaxed, ground state atomic configuration of each of the systems was generated, they were used as the perfect cell for Phonopy. Then, atomic configuration files are generated where each atom is individually displaced by the default atomic displacement distance of 0.01 Å. The size of the displacement is an important consideration when the accuracy of the force calculation cannot be easily controlled. However, in VASP, the accuracy of the calculation can be well controlled and the default value of the displacement was deemed appropriate [76], [77].

For constant volume heat capacity, only one volume with its corresponding vibrations is necessary. For constant pressure heat capacity, thermal expansion, and the Grüneisen Parameter, five volumes are necessary; two volumes above and two below (2.5% and 5% larger and smaller) along with the ground state volume are necessary. The supercell approach, which repeated the unit cell into a larger supercell, was not used for the hydrate structures. Using a $2 \times 2 \times 2$ supercell, which would remove possible effects from the periodicity of the atomic displacement in the unit cell, would multiply the number of atoms by eight and the computational time by an order of magnitude. Testing revealed that the computational time would increase from four core years to forty core years per volume. Each structure required calculations at five volumes, and since five structures were tested (four hydrates and hexagonal ice). Therefore, the total computational time would increase from approximately 100 core-years to 1000 core-years, a number exceeding the computational time available.

However, because the hexagonal Bernal-Fowler ice unit cell contains 36 atoms, using a $2 \times 2 \times 2$ supercell just for the ice structure gave 288 atoms, slightly higher than 202 atoms contained in the ethane unit cell, the one with the most atoms. This enabled the usage of the same parallelization parameters and the difference was counterbalanced by the increase in memory

requirements for the calculation which did not impact overall computational time. Additionally, the number of displacements to calculate is much lower, so the total computational time required is lower than the hydrate structures.

With the atomic configurations generated, it became necessary to then calculate the force and energy increase corresponding to each atomic configuration. This force/energy calculation was performed with VASP.

3.4 Force/Energy Calculation

The Vienna Ab Initio Simulation Package (VASP) is a package that performs ab-initio quantum-mechanical molecular dynamics simulations. It performs these calculations using the projector-augmented wave method and a plane wave basis set or pseudopotentials [61]. Using an efficient Pulay/Broyden charge density mixing and efficient matrix diagonalization schemes, VASP is able to exactly evaluate the instantaneous electronic ground state with free energy as the varying quantity at each calculation time step, avoiding problems present in the Car-Parrinello method, which simultaneously integrates ionic and electronic equations of motion [61], [78]–[81]. It relaxes atoms to their ground state by calculating and using forces and full stress tensors. By describing the interaction between ions and electrons by the projector-augmented wave method or ultra-soft Vanderbilt pseudopotentials, VASP can considerably reduce the number of plane-waves per atom for first row elements and transition metals [78], [82]. The Vienna Ab Initio Simulation Package can use a large amount of input files, although at least four specific ones are necessary: INCAR, KPOINTS, POSCAR, and POTCAR.

The parameters of the INCAR file that were important to the force/energy calculation were: the precision mode, the plane wave energy cut off, the tolerance of the electronic energy

calculation, and the exchange correlation functional to be used. The most accurate precision mode was used. This mode uses an augmentation grid that is twice as fine at the grid that is used for the pseudo orbitals. It also rigorously avoids wrap around errors and possible aliasing. This precision mode is also the one recommended for phonon calculations [83]. The plane wave energy cut off used was 520 eV, 30% higher than the highest cut off 400 eV provided in the pseudopotentials by VASP, and helpful for counter-acting the displacement distance chosen during preprocessing [84]. The electronic energy tolerance used was 10^{-8} eV, as used by the creators of Phonopy [76] and the exchange correlation function used was, as explained in section 3.1, the SCAN + rVV10 functional.

The POSCAR files are the atomic configurations generated during preprocessing. The POTCAR files are pseudopotential files corresponding to each atom species present in each calculation and provided by the VASP developers. In this case and per the recommendation of the developers, the projector augmented wave potentials were employed [85], [86]. The KPOINTS defined the k-point grid to be used. For the sI hydrate and the number of atoms per unit cell, a $3 \times 3 \times 3$ Gamma-centered mesh, producing a mesh containing 14 k-points, was used, consistent with other studies of gas hydrates of similar size and number of atoms [5], [22], [41].

Other parameters are available and necessary in the INCAR file, but these affect the speed and stability of convergence (not the force/energy calculation), and are explained in section 3.6.

3.5 Postprocessing

VASP calculates and outputs the force constants and total energy of the system for each of the displacements. In postprocessing, Phonopy is used once again. Calculating the constant volume heat capacity involves using the harmonic approximation. By presuming it is a function of atomic

displacement, the crystal potential energy can be expanded as a Taylor Series. By using small displacements at constant volume, the first and second order terms can be treated with the harmonic approximation, while higher orders terms can be treated by perturbation theory. With the crystal potential defined, the dynamic properties of atoms can be calculated, which in turn yields the phonon frequencies over the Brilluoin Zone. These phonon frequencies, along with the canonical distribution of statistical mechanics, can be used to calculate the constant volume heat capacity for the given crystal structure [76]. By taking the total energies and force constants in the output files from VASP, Phonopy calculates these properties. The constant volume heat capacity was calculated in one-degree increments from zero Kelvin to 300 Kelvin with a q-point mesh of $30 \times 30 \times 30$ centered on the Gamma point.

The constant pressure heat capacity, the thermal expansion, and the Grüneisen all depend on the volume of the crystal. By applying the quasi-harmonic approximation, where the harmonic approximation is applied at specific volumes, these thermal properties can be calculated. To do this, the Gibbs Free Energy at a given temperature and pressure is calculated from the Helmholtz free energy, which itself is derived from the phonon frequencies. Then, fundamental thermodynamics can be used to transform the constant volume heat capacity to constant pressure heat capacity by calculating the contribution to heat capacity from thermal expansion. The thermal expansion can be calculated from the derivative of volume as a function of temperature. The Grüneisen parameter can be calculated from the dynamic properties of the atoms [76], [87]. These properties calculated in one-degree increments from zero Kelvin to 300 Kelvin with a q-point mesh of $30 \times 30 \times 30$ centered on the Gamma point.

3.6 Computational Details

All the calculations for this research project were conducted on the Compute Canada network of supercomputing clusters. The specific computers used were Cedar, Graham, and Béluga. The workload was spread across nodes of 32 (Cedar, Graham) or 40 (Béluga) cores. Four nodes were used for the gas hydrates, and three were used for the hexagonal ice structure. After testing, and with confirmation from HPC data concerning VASP, this number of total cores allowed for the best parallel efficiency in these calculations [88], [89].

VASP allows the users to select certain parameters related to parallelization of the calculation more importantly than to the numerical calculation itself. The number of cores that work on an orbital, NCORE, was set to 40 or 32 depending on the number of cores available on the nodes employed, as suggested by the VASP developers for multicore machines linked by very fast networks [88]. The plane-wise distribution was set to real space via LPLANE thanks to the same recommendation [90]. Gaussian smearing was used (ISM EAR) with a smearing width of 0.01 eV [91], [92]

4 Results and Discussion

This section presents the calculated constant volume heat capacity, constant pressure heat capacity, thermal expansion coefficient, and the Grüneisen parameter with appropriate discussion.

4.1 Constant Volume Heat Capacity

The constant volume heat capacity of the ethane, methane, carbon dioxide, and empty hydrates, and hexagonal ice is plotted as a function of temperature in Figure 4-1. Molecular dynamics simulations from literature of the same property are also plotted.

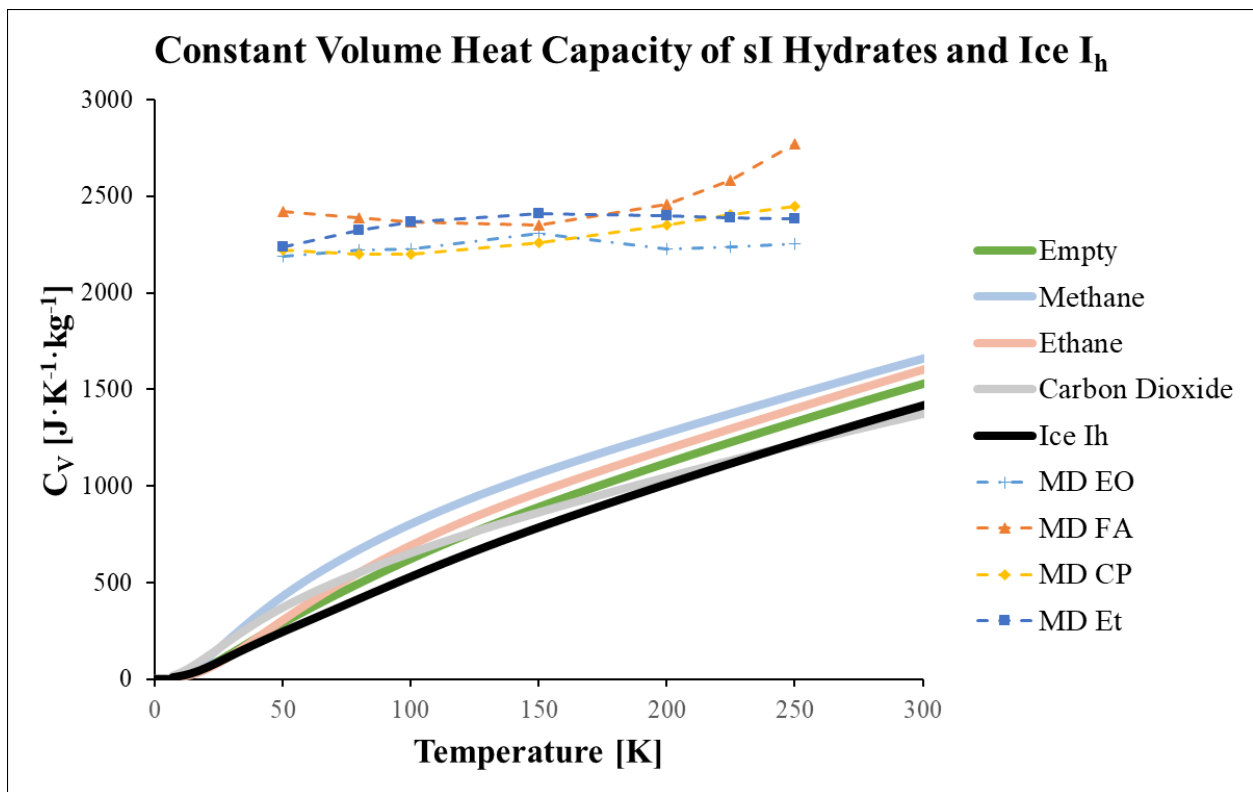


Figure 4-1: Heat Capacity of sI Hydrates and Ice I_h Computed with DFT (solid lines) and molecular dynamics (MD) [54] with Various Guest Molecules: EO (ethylene oxide), FA (formaldehyde), CP (cyclopentane), and Et (ethane)

As seen in Figure 4-1, the DFT results show similar trends regardless of guest molecule. The values are similar to hexagonal ice throughout the temperature range. Because this heat capacity is measured at constant volume, there is no hydrate cage expansion. If heat capacity trends are structure related, the differentiation cannot be seen with constant volume heat capacity.

Methane hydrates have the highest heat capacity of this type because of the ability of the methane molecule to rotate freely in the hydrate structure, an additional degree of freedom. This is confirmed by the lack of ionic optimization with regards to the methane molecule orientation and by X-ray diffraction [70]. The next highest hydrate, according to DFT, is the ethane hydrate (beyond 70 Kelvin). This is because of the ability of the two methyl groups and their degrees of freedom. It does not have as many possibilities for movement, vibration, or rotation because of its size which causes it to be oriented along the hexagonal face of the large cage, a finding that will be discussed later in section 4.3.

The third highest structure is the empty hydrate backbone. As expected, at very low temperatures it has the smallest heat capacity and it nearly equal to ice. However, as temperature increases this behavior deviates and it falls in line with the trend of other hydrates. It is also expected that it has the lowest heat capacity out of the hydrates, except for carbon dioxide, because it possesses the least degrees of freedom by virtue of not having a guest molecule. Hexagonal ice is the closest to the hydrate backbone. Its heat capacity is lower than the backbone because it possesses less degrees of freedom in its structure, with less edges and vertices in the structure to bend and stretch.

The carbon dioxide hydrate has a heat capacity equal to that of the methane hydrate before 50 Kelvin. However, it shows a decreased in its slope as temperature increases, eventually going

lower than hexagonal ice at 250 Kelvin. This would indicate that the guest molecule interacts with the hydrate backbone to create a system with less degrees of freedom than the ethane hydrate and that over time it cannot vibrate, move, or rotate as much. While carbon dioxide, being double bonded triatomic linear molecule as opposed to ethane, has less degrees of freedom, it still goes against the shown trend with the other hydrates.

Molecular dynamics studies of the constant volume heat capacity are also shown in Figure 4-1. They were performed for guest molecules of varying polarity and structure using a $3 \times 3 \times 3$ replica of the hydrate unit cells [54]. The results of those studies produced heat capacities between 200% and 500% higher than those produced by DFT. Also, these studies showed that the heat capacity is a much weaker function of temperature. Like this research project, the molecular dynamics study showed overall small variations in heat capacity with guest type and electron density (for example, methane versus carbon dioxide or ethane versus ethylene oxide). Without experimental constant volume heat capacity, it is difficult to establish a preferred or more accurate methodology. Constant pressure heat capacity presents a better quantity that is easier to measure in the lab.

4.2 Constant Pressure Heat Capacity

The constant pressure heat capacity of the empty hydrate backbone, the methane, ethane, and carbon dioxide hydrate, and hexagonal ice is plotted as a function of temperature in Figure 4-2. Molecular dynamics simulations and experimental values from literature of the same property are also plotted.

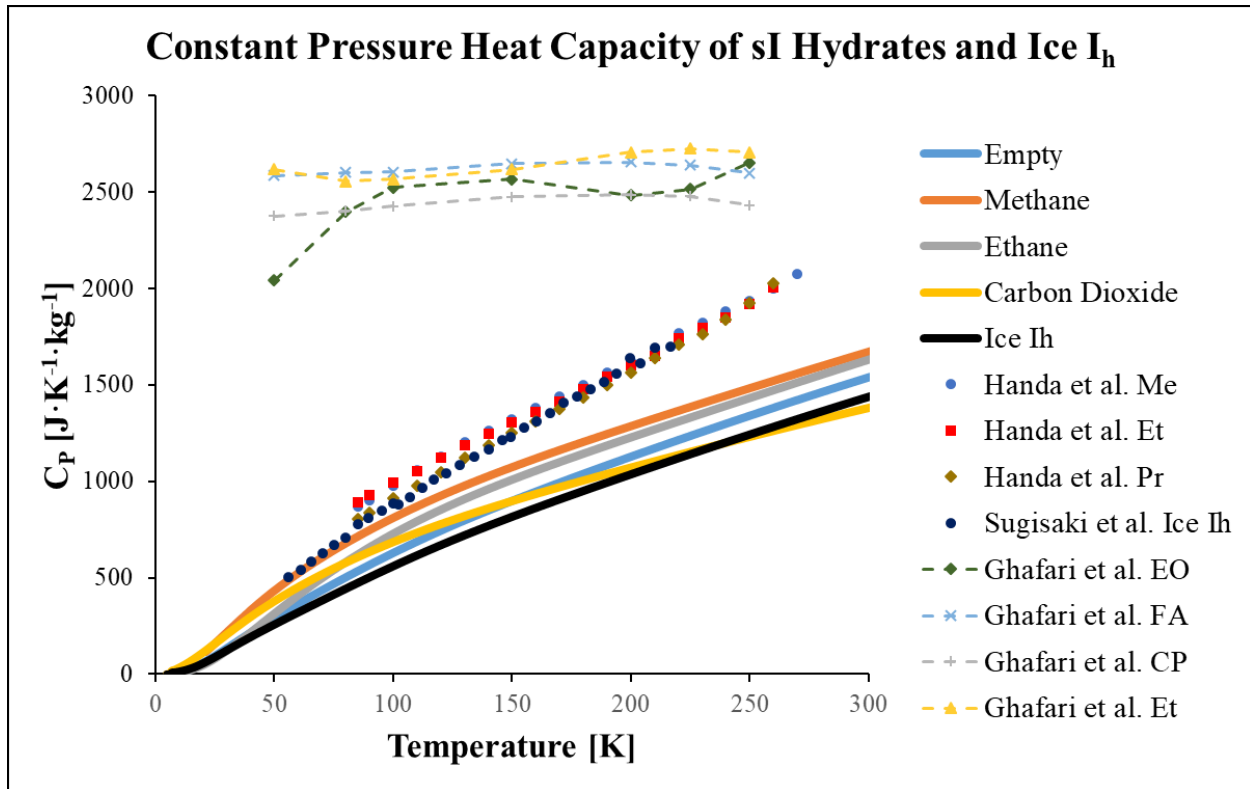


Figure 4-2: Heat Capacity of sI Hydrates and Ice I_h Computed with DFT (solid lines), Experiment [55], [93] (points), and Molecular Dynamics (MD) [54] (dashed lines) with Various Guest Molecules: EO (ethylene oxide), FA (formaldehyde), CP (cyclopentane), and Et (ethane), Me (methane), Pr (propane)

Figure 4-2 shows very similar trends to Figure 4-1. DFT results show similar trends regardless of the guest molecule. Methane hydrates have the highest heat capacity because they have more degrees of freedom. The ethane hydrate is the second highest heat capacity and the carbon dioxide hydrate shows the same deviation as in the constant volume case.

When compared to Figure 4-1, Figure 4-2 is consistent with fundamental thermodynamics. The difference between the constant volume heat capacity and the constant pressure heat capacity is the thermal expansion contribution, which for solids is usually low. The difference between the two capacities is less than 5% across the range of presented temperatures and constant pressure heat capacity is always higher, consistent with fundamental thermodynamics [76]. In the constant

pressure case, the ethane hydrate approaches the methane hydrate heat capacity at higher temperatures because the structure is expanding due to the temperature. This allows the ethane hydrate to move more freely compared to lower temperature states, augmenting the degrees of freedom of the ethane molecule. Once again, the hydrates have similar heat capacities to hexagonal ice. The difference lies in the containment of a guest molecule, which increases the degrees of freedom of the structure, allowing for more energy storage.

Constant pressure heat capacity can be more easily measured in the laboratory setting and Figure 4-2 presents experimental data for ice and methane, ethane, and propane hydrates. Experimental data shows that hydrates and ice have very similar heat capacities. Experiments also show that the correlation with temperature is linear. At approximately 50 Kelvin, the DFT results deviate from the trend of experimental data and after this point, the heat capacity shows a weaker correlation with temperature. Even though the goal is to use thermodynamics to extend information obtained from the zero-Kelvin environment of DFT to real temperatures, it is important to remember that the basis is still a zero-Kelvin structure and, in this case, DFT is resolving temperature effects that have become averaged out or cancelled by other phenomena that it cannot capture.

Molecular dynamics studies of the constant pressure heat capacity are also shown in Figure 4-2. The results of those studies produced heat capacities that 200% and 500% higher than those produced by this research project and showed that the heat capacity is a weak function of temperature. Like this research project, the molecular dynamics studies showed overall small variations in heat capacity with guest type and electron density. These studies show poor agreement with experiment across all temperatures. The correlation with temperature is much weaker and the values are overestimated. Although molecular dynamics can be stronger at higher

temperatures, it does not indicate a change in trend that would allow it to replicate experimental data as well as DFT.

4.3 Thermal Expansion Coefficient

The thermal expansion coefficient of the empty hydrate backbone, the methane, ethane, and carbon dioxide hydrate, and hexagonal ice is plotted as a function of temperature in Figure 4-3. Molecular dynamics simulations and experimental values from literature of the same property are also plotted. Figure 4-4 presents only the thermal expansion calculated with DFT for discussion and examination purposes.

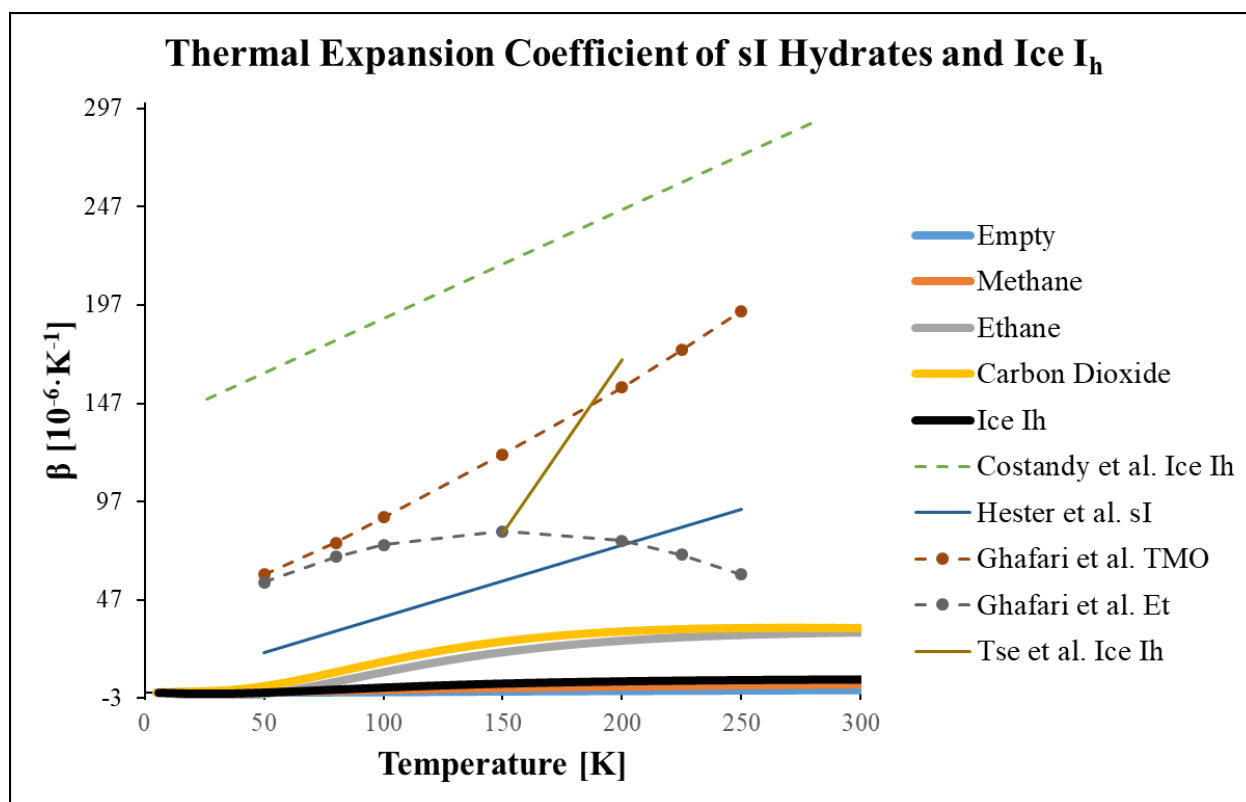


Figure 4-3: Volumetric Thermal Expansion of sI Hydrates and Ice I_h Computed with DFT (thick solid lines), molecular dynamics (MD) [54], [94] (dashed lines), and Experiment [95], [96] (solid lines)

Figure 4-3 confirms the adherence to traditional solid trends for heat capacity. Since the thermal expansion coefficient is so small, the expansion contribution to constant pressure heat capacity is very low, leaving it nearly equal to the constant volume heat capacity. Figure 4-3 also shows that DFT vastly underestimates the thermal expansion coefficient of gas hydrates and ice when compared to the experimentally determined average expansion of sI hydrates. One set of molecule dynamics measurements shows two different trends. [54] shows that at low temperature, trimethyl oxide and ethane hydrate have very similar heat capacity, but as the temperature increases, the ethane hydrate has a decreasing thermal expansion. This trend goes against that which has been calculate with DFT and against the experimental values for sI hydrates. Also, molecule dynamics studies do not display the negative thermal expansion behavior close to zero Kelvin, while experimental sI hydrates do. Experimentally, hexagonal ice has been shown to have negative thermal expansion at very low temperatures [97], but there is a lack, due to technical difficulties, of very low temperature measurements [96]. To examine the DFT calculations further, the molecular dynamics and experimental studies will be omitted in Figure 4-4 for visual clarity.

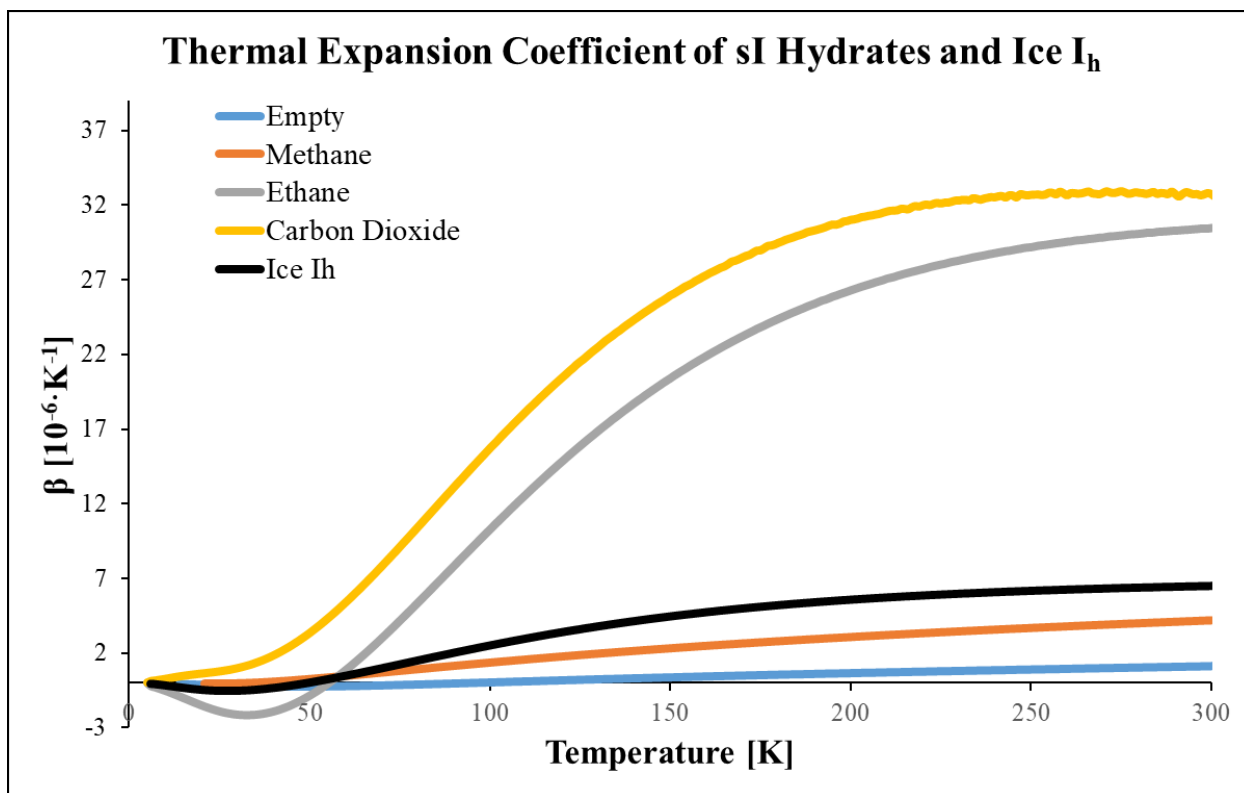


Figure 4-4: Volumetric Thermal Expansion Coefficient of sI Hydrates and Ice I_h Computed With DFT

Figure 4-4 displays the negative thermal expansion at low temperatures for hexagonal ice, as well as for the empty, ethane, and methane hydrates. The calculated thermal expansion of the ethane and carbon dioxide hydrates was higher than hexagonal ice, while the empty hydrates and the methane hydrate were lower than hexagonal ice beyond 50 Kelvin. This is in contrast to another DFT study, which found the thermal expansion of the carbon dioxide hydrate to be lower than that of hexagonal ice [24]. The empty and methane hydrates are much closer to ice than carbon dioxide and ethane hydrates because, structurally, they are most like ice. The methane in the hydrate is small enough that thermal expansion or contract does not constrain it and make it interact strongly with the backbone. The carbon dioxide and ethane hydrates have thermal expansions that are

initially much more sensitive to temperature but plateau at 240 Kelvin. This difference is due to their equilibrium structures, presented in Figure 4-5 from the same view.

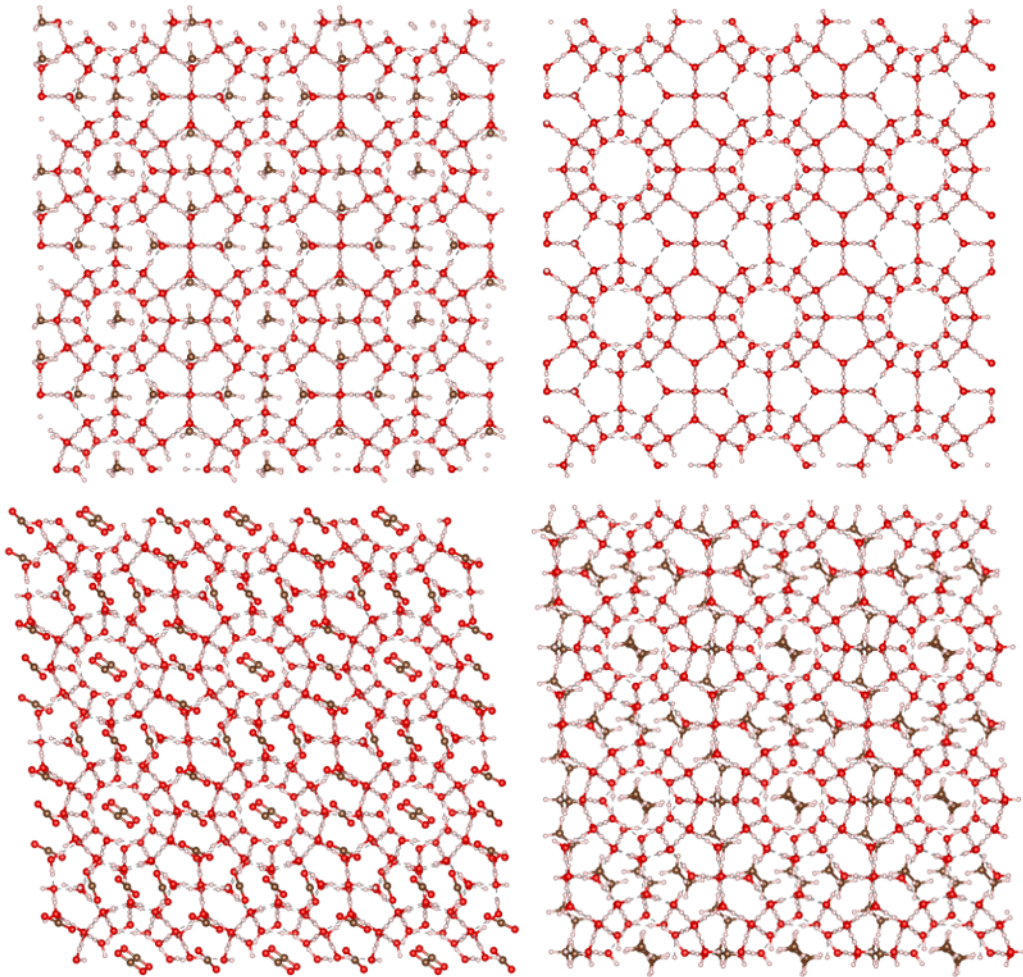


Figure 4-5: Methane Hydrate (top left), Empty Hydrate (top right), Carbon Dioxide Hydrate (bottom left), ethane hydrate (bottom right) Viewed Through the Hexagonal Face of the $5^{12}6^2$ Cages, Generated with VESTA Visualization Software [98]

Figure 4-5 shows three unit cells for all the equilibrated hydrate systems considered. Each equilibrated system deviated at most by 0.5%, in terms of lattice parameters (but not angles), from the hydrate backbone. The methane hydrate's backbone remains unchanged when compared to the empty hydrate. In stark contrast, the carbon dioxide hydrate shows an alignment of all guest

molecules. All molecules showed the same rotation with respect to the viewing plane, leading to the conclusion that they are constrained in one aspect to be oriented to a plane parallel to the hexagonal faces of the $5^{12}6^2$ cages. Guest molecules not located in those cages are oriented along planes that are nearly parallel to the hexagonal face planes. This finding confirms other DFT findings for the carbon dioxide hydrate [99]. However, this research project also shows that depending on which cage the guest molecule is located in, its orientation is additionally fixed to minimize the energy of the system. Figure 4-5 shows that all molecules align themselves in a similar direction to minimize the total energy of the system, although this does not mean a completely parallel alignment for all molecules. The same findings shown for the carbon dioxide hydrate are true for the ethane hydrate system. However, the ethane molecule has a smaller effect on the hydrate backbone.

These findings help explain the trends seen in Figure 4-4. Because the ethane and carbon dioxide molecules significantly change their host lattice, they will have thermal expansion coefficients that are more sensitive to temperature. The host lattice will behave differently in the presence of a larger guest molecule. This indicates the presence of stronger guest-host interactions than in the methane hydrate case. The plateau seen for both these hydrates at higher temperatures indicated that, as the hydrate expands, the incremental effect of the guest-host interactions diminishes.

4.4 Grüneisen Parameter

The Grüneisen parameter of the empty hydrate backbone, the methane, ethane, and carbon dioxide hydrate, and hexagonal ice is plotted as a function of temperature along with experimentally determined values for the parameter [96], in Figure 4-6. The Grüneisen parameter

is used to explain the effect on vibrational and thermal properties introduced by a volume change, and as such explains how temperature affects these properties by affecting volume. It is also useful to set theoretical limits on parameters and allows for the estimation of the temperature dependence of thermal properties [100].

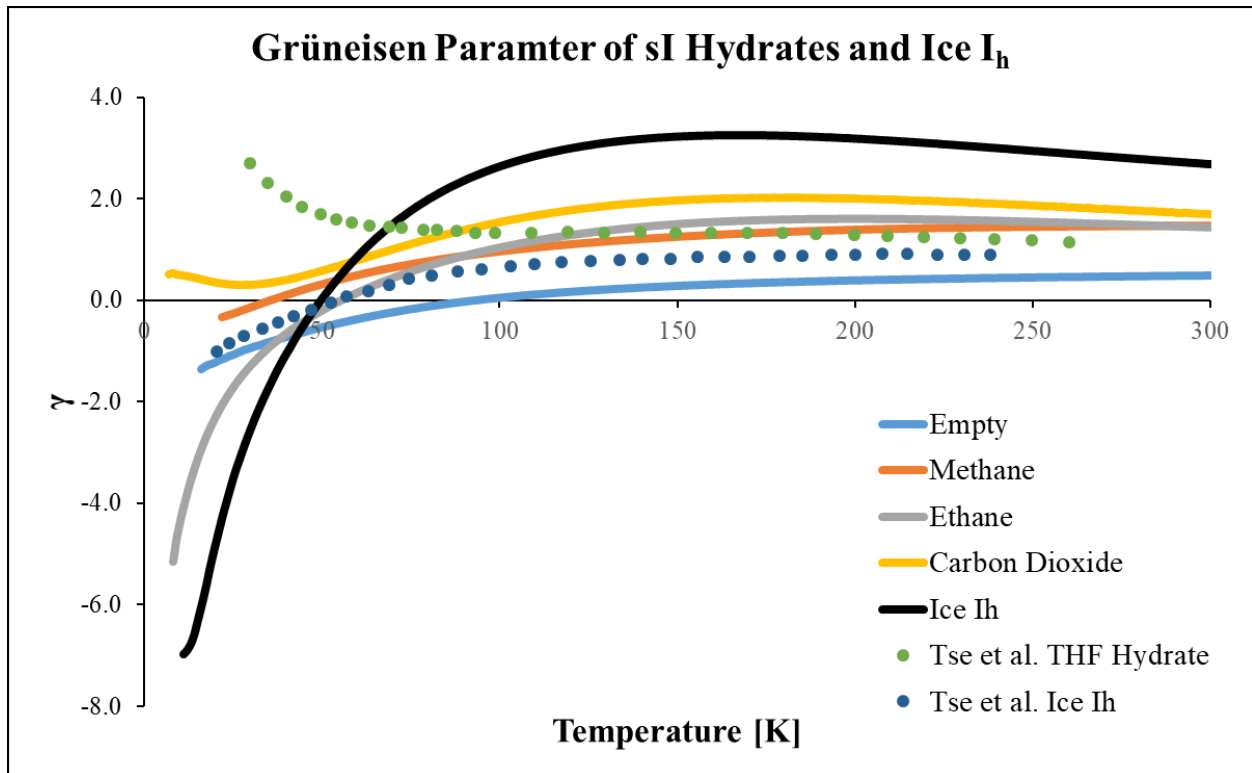


Figure 4-6: Grüneisen Parameter of sI Hydrates and Ice I_h Computed with DFT (solid lines) and Experimentally Determined for THF Hydrates and Ice I_h (points) [96]

Figure 4-6 shows the similar behavior for all sI hydrates except for the carbon dioxide hydrate. All filled hydrates approach a Grüneisen parameter of 1.7 as the temperature increases. All systems of interest in this study follow similar trends after approximately 40 Kelvin. There is a continued increase in the Grüneisen parameter followed by a plateau and approach towards a constant. The approach to a constant value is consistent with experimental data for hydrates and most materials in general [96], [100]. The empty hydrate approaches a smaller value of 0.5 at 300

Kelvin. The carbon dioxide hydrate does not have a negative Grüneisen parameter. Because one of the formulations of the Grüneisen parameter is based on the thermal expansion coefficient, the exclusively positive behavior of the carbon dioxide system is tied to the exclusively positive thermal expansion coefficient of the hydrate.

Experimental values for the sII tetrahydrofuran (THF) hydrate show behavior that does against the results calculated with DFT. The unusual behavior has been seen in crystals doped with impurities as well as disordered materials [101]. However, gas hydrates are not disordered materials, due to their periodic and crystalline nature. The general trend towards a constant value is consistent with DFT, but the approach is not. The same study presents values for hexagonal ice. The Grüneisen parameter is lower experimentally beyond 40 Kelvin. The DFT gas hydrates behave more like the experimental hexagonal ice than the calculated hexagonal ice. If ice samples have impurities, they may seem to behave like hydrates because hydrates are nearly hexagonal ice containing guest molecules. The empty hydrate behaved the most closely like the experimental hexagonal ice.

5 Conclusion

To conclude this study, the main findings will be reviewed and recommendations for future work will be given based on these findings and their potential applications.

The constant volume heat capacity, the constant pressure heat capacity, the volumetric thermal expansion coefficient, and the Grüneisen parameter of methane, ethane, carbon dioxide, and empty sI hydrates, and of hexagonal ice, as functions of temperature from 0 to 300 Kelvin were calculated using DFT. The constant volume heat capacity calculated with DFT was lower than when compared with literature values calculated with MD, and the trends with respect to temperature much stronger in the positive direction. The constant pressure heat capacity with DFT was also lower than literature values calculated with MD. However, DFT replicated experimental values for hydrates and ice well at low temperatures. DFT also show similar trends when compared to experimental values of the heat capacity. The volumetric thermal expansion coefficient was calculated and compared to experiment and MD simulations. DFT underestimated the coefficient in all cases. The ethane and carbon dioxide hydrates demonstrated behavior that was markedly different when compared to methane and empty hydrates, and hexagonal ice. The thermal expansion coefficient was much lower. Overall, the thermal expansion coefficient showed that the difference between the constant volume and constant pressure heat capacity should be small, which is was. The Grüneisen parameter was calculated for all systems. DFT overestimates the value of the parameter for filled hydrates and hexagonal ice when compared to experimental hexagonal ice values.

This research study accomplished the principal objective of calculated these quantities of interest with respect to temperature. This work adequately used computational techniques to use

atomic configuration information to simulate macroscopic, real world thermal properties in a zero-Kelvin computational setting. Using fundamental thermodynamics as implemented in Phonopy, DFT was able to predict these properties without using empirically determined parameters specific to gas hydrates or ice.

One future avenue of work involves closing the gap with experimental data. DFT seems to resolve temperature effects as temperature increases which may not be presented anymore or may be cancelled out by other effects. The thermodynamic framework used to extend the simulation vibrations could be improved by considering more information, such as by utilizing a large supercell when available computational power provides an opportunity to do so. Another future avenue of work involves calculating the thermal conductivity of gas hydrates. Even when using the smallest amount of additional interactions necessary for the calculation to go beyond heat capacity, the computation time required increases by at least an order of magnitude. It is not possible to reduce this time with the same level of accuracy in this study because of the size of the unit cell of gas hydrates. Because this work utilized phonon properties and frequencies, it is possible to predict a variety of spectra for gas hydrates as well. Computationally, there are still various avenues to explore for these gas hydrates.

6 References

- [1] M. D. Max, *Natural Gas Hydrate in Oceanic and Permafrost Environments*. Springer Science & Business Media, 2003.
- [2] J. Carroll, *Natural Gas Hydrates: A Guide for Engineers*, 3rd ed. Gulf Professional Publishing, 2014.
- [3] C. Koh, E. Dendy Sloan, A. Sum, and D. Wu, *Fundamentals and Applications of Gas Hydrates*, vol. 2. 2011.
- [4] U. Tinivella, M. Giustiniani, I. de la C. Vargas Cordero, and A. Vasilev, “Gas Hydrate: Environmental and Climate Impacts,” *Geosciences*, vol. 9, no. 10, p. UNSP 443, Oct. 2019, doi: 10.3390/geosciences9100443.
- [5] Z. M. Jendi, A. Rey, and P. Servio, “Ab initio DFT study of structural and mechanical properties of methane and carbon dioxide hydrates,” *Mol. Simul.*, vol. 41, May 2015, doi: 10.1080/08927022.2014.899698.
- [6] A. Demirbas, *Methane Gas Hydrate*. Springer Science & Business Media, 2010.
- [7] M. Gudala, “Modelling of methane hydrate formation and dissociation in presence of surfactants by chemical affinity,” 2013.
- [8] Z. Sun *et al.*, “Effect of cage-specific occupancy on the dissociation rate of a three-phase coexistence methane hydrate system: A molecular dynamics simulation study,” *J. Nat. Gas Sci. Eng.*, vol. 55, pp. 235–242, Jul. 2018, doi: 10.1016/j.jngse.2018.05.004.
- [9] J. Rajnauth, M. Barrufet, and G. Falcone, “Potential Industry Applications Using Gas Hydrate Technology,” 2010, doi: 10.2523/133466-MS.
- [10] David Wolman and Adam Friedberg, “Hydrates, Hydrates Everywhere | DiscoverMagazine.com,” *Discover Magazine*, 01-Oct-2004.
- [11] C. Cheng *et al.*, “Review and prospects of hydrate cold storage technology,” *Renew. Sustain. Energy Rev.*, vol. 117, p. 109492, Jan. 2020, doi: 10.1016/j.rser.2019.109492.
- [12] B. Tohidi, R. Anderson, H. Mozaffar, and F. Tohidi, “The Return of Kinetic Hydrate Inhibitors,” *Energy Fuels*, vol. 29, no. 12, pp. 8254–8260, Dec. 2015, doi: 10.1021/acs.energyfuels.5b01794.
- [13] A. Mandal and S. Laik, “Effect of the Promoter on Gas Hydrate Formation and Dissociation,” *Energy Fuels*, vol. 22, no. 4, pp. 2527–2532, Jul. 2008, doi: 10.1021/ef800240n.
- [14] U. Karaaslan and M. Parlaktuna, “Promotion Effect of Polymers and Surfactants on Hydrate Formation Rate,” *Energy Fuels*, vol. 16, no. 6, pp. 1413–1416, Nov. 2002, doi: 10.1021/ef020023u.
- [15] D. Mech, P. Gupta, and J. S. Sangwai, “Kinetics of methane hydrate formation in an aqueous solution of thermodynamic promoters (THF and TBAB) with and without kinetic promoter

- (SDS),” *J. Nat. Gas Sci. Eng.*, vol. 35, pp. 1519–1534, Sep. 2016, doi: 10.1016/j.jngse.2016.06.013.
- [16] L. Yang *et al.*, “The status of exploitation techniques of natural gas hydrate,” *Chin. J. Chem. Eng.*, vol. 27, no. 9, pp. 2133–2147, Sep. 2019, doi: 10.1016/j.cjche.2019.02.028.
- [17] S. Merey and S. N. Longinos, “The gas hydrate potential of the Eastern Mediterranean basin,” *Bull. Miner. Res. Explor.*, vol. 160, pp. 117–133, 2019, doi: 10.19111/bulletinofmre.502275.
- [18] E. D. Sloan, “Gas Hydrates: Review of Physical/Chemical Properties,” *Energy Fuels*, vol. 12, no. 2, pp. 191–196, Mar. 1998, doi: 10.1021/ef970164+.
- [19] A. A. Khokhar, J. S. Gudmundsson, and E. D. Sloan, “Gas storage in structure H hydrates,” *Fluid Phase Equilibria*, vol. 150–151, pp. 383–392, Sep. 1998, doi: 10.1016/S0378-3812(98)00338-0.
- [20] S. M. Daghash, P. Servio, and A. D. Rey, “Structural properties of sH hydrate: a DFT study of anisotropy and equation of state,” *Mol. Simul.*, vol. 45, no. 18, pp. 1524–1537, Dec. 2019, doi: 10.1080/08927022.2019.1660326.
- [21] G. Winckler *et al.*, “Noble gases and radiocarbon in natural gas hydrates,” *Geophys. Res. Lett.*, vol. 29, no. 10, pp. 63-1-63-4, doi: 10.1029/2001GL014013.
- [22] T. M. Vlastic, P. D. Servio, and A. D. Rey, “Effect of Guest Size on the Mechanical Properties and Molecular Structure of Gas Hydrates from First-Principles,” *Cryst. Growth Des.*, vol. 17, no. 12, pp. 6407–6416, Dec. 2017, doi: 10.1021/acs.cgd.7b01072.
- [23] R. P. Warzinski *et al.*, “Thermal Properties of Methane Hydrate by Experiment and Modeling and Impacts Upon Technology,” in *Alternative Energy and Shale Gas Encyclopedia*, Wiley-Blackwell, 2016, pp. 680–686.
- [24] Z. Jendi, P. Servio, and A. Rey, “Ab Initio Modelling of Methane Hydrate Thermophysical Properties,” *Phys Chem Chem Phys*, vol. 18, Mar. 2016, doi: 10.1039/C5CP06530E.
- [25] E. J. Rosenbaum, N. J. English, J. K. Johnson, D. W. Shaw, and R. P. Warzinski, “Thermal Conductivity of Methane Hydrate from Experiment and Molecular Simulation,” *J. Phys. Chem. B*, vol. 111, no. 46, pp. 13194–13205, Nov. 2007, doi: 10.1021/jp074419o.
- [26] J. M. Schicks, J. Erzinger, and M. A. Ziemann, “Raman spectra of gas hydrates—differences and analogies to ice 1h and (gas saturated) water,” *Spectrochim. Acta. A. Mol. Biomol. Spectrosc.*, vol. 61, no. 10, pp. 2399–2403, Aug. 2005, doi: 10.1016/j.saa.2005.02.019.
- [27] S. B. Hansen and R. W. Berg, “Raman Spectroscopic Studies of Methane Gas Hydrates,” *Appl. Spectrosc. Rev.*, vol. 44, no. 2, pp. 168–179, Feb. 2009, doi: 10.1080/05704920802352614.
- [28] J. Qin and W. F. Kuhs, “Quantitative analysis of gas hydrates using Raman spectroscopy,” *AIChE J.*, vol. 59, no. 6, pp. 2155–2167, Jun. 2013, doi: 10.1002/aic.13994.
- [29] F. Rauh, J. Pfeiffer, and B. Mizaikoff, “Infrared spectroscopy on the role of surfactants during methane hydrate formation,” *RSC Adv.*, vol. 7, no. 62, pp. 39109–39117, Aug. 2017, doi: 10.1039/C7RA05242A.

- [30] E. D. S. Jr and C. Koh, *Clathrate Hydrates of Natural Gases, Third Edition*. CRC Press, 2007.
- [31] M. Maslin, M. Owen, R. Betts, S. Day, T. D. Jones, and A. Ridgwell, “Gas hydrates: past and future geohazard?,” *Philos. Trans. R. Soc. Lond. Math. Phys. Eng. Sci.*, vol. 368, no. 1919, pp. 2369–2393, May 2010, doi: 10.1098/rsta.2010.0065.
- [32] J.-L. Kuo, J. Coe, S. Singer, Y. Band, and L. Ojamäe, “On the use of graph invariants for efficiently generating hydrogen bond topologies and predicting physical properties of water clusters and ice,” *Chem. Phys. - CHEM PHYS*, vol. 114, pp. 2527–2540, Feb. 2001, doi: 10.1063/1.1336804.
- [33] J. G. Beltran, H. Bruusgaard, and P. Servio, “Gas hydrate phase equilibria measurement techniques and phase rule considerations,” *J. Chem. Thermodyn.*, vol. 44, no. 1, pp. 1–4, Jan. 2012, doi: 10.1016/j.jct.2011.08.026.
- [34] S. Subramanian, A. L. Ballard, R. A. Kini, S. F. Dec, and E. D. Sloan, “Structural transitions in methane+ethane gas hydrates — Part I: upper transition point and applications,” *Chem. Eng. Sci.*, vol. 55, no. 23, pp. 5763–5771, Dec. 2000, doi: 10.1016/S0009-2509(00)00162-7.
- [35] O. Y. Zatsepina and B. A. Buffett, “Phase equilibrium of gas hydrate: Implications for the formation of hydrate in the deep sea floor,” *Geophys. Res. Lett.*, vol. 24, no. 13, pp. 1567–1570, doi: 10.1029/97GL01599.
- [36] P. Zhang, Q. Wu, and C. Mu, “Influence of temperature on methane hydrate formation,” *Sci. Rep.*, vol. 7, Aug. 2017, doi: 10.1038/s41598-017-08430-y.
- [37] M. B. Helgerud, W. F. Waite, S. H. Kirby, and A. Nur, “Measured temperature and pressure dependence of compressional (V_p) and shear (V_s) wave speeds in compacted, polycrystalline ice Ih,” *Can. J. Phys.*, vol. 81, no. 1–2, pp. 81–87, Jan. 2003, doi: 10.1139/p03-008.
- [38] M. B. Helgerud, W. F. Waite, S. H. Kirby, and A. Nur, “Measured temperature and pressure dependence of V_p and V_s in compacted, polycrystalline sI methane and sII methane–ethane hydrate,” *Can. J. Phys.*, vol. 81, no. 1–2, pp. 47–53, Jan. 2003, doi: 10.1139/p03-016.
- [39] M. B. Helgerud, W. F. Waite, S. H. Kirby, and A. Nur, “Elastic wave speeds and moduli in polycrystalline ice Ih, sI methane hydrate, and sII methane-ethane hydrate,” *J. Geophys. Res. Solid Earth*, vol. 114, no. B2, Feb. 2009, doi: 10.1029/2008JB006132.
- [40] H. Huo, Y. Liu, Z. Zheng, J. Zhao, C. Jin, and T. Lv, “Mechanical and thermal properties of methane clathrate hydrates as an alternative energy resource,” *J. Renew. Sustain. Energy*, vol. 3, Dec. 2011, doi: 10.1063/1.3670410.
- [41] Z. M. Jendi, P. Servio, and A. D. Rey, “Ideal Strength of Methane Hydrate and Ice Ih from First-Principles,” *Cryst. Growth Des.*, vol. 15, no. 11, pp. 5301–5309, Nov. 2015, doi: 10.1021/acs.cgd.5b00829.
- [42] C. R. Miranda and T. Matsuoka, “First-principles study on mechanical properties of CH₄ hydrate,” presented at the 6th International Conference on Gas Hydrates, Vancouver, BC, 2008, doi: 10.14288/1.0041001.

- [43] H. Shimizu, T. Kumazaki, T. Kume, and S. Sasaki, “Elasticity of single-crystal methane hydrate at high pressure,” *Phys. Rev. B*, vol. 65, no. 21, p. 212102, May 2002, doi: 10.1103/PhysRevB.65.212102.
- [44] R. Sakamaki, A. K. Sum, T. Narumi, R. Ohmura, and K. Yasuoka, “Thermodynamic properties of methane/water interface predicted by molecular dynamics simulations,” *J. Chem. Phys.*, vol. 134, no. 14, p. 144702, Apr. 2011, doi: 10.1063/1.3579480.
- [45] P. Naeiji, F. Varaminian, and M. Rahmati, “Thermodynamic and structural properties of methane/water systems at the threshold of hydrate formation predicted by molecular dynamic simulations,” *J. Nat. Gas Sci. Eng.*, vol. 31, pp. 555–561, Apr. 2016, doi: 10.1016/j.jngse.2016.03.044.
- [46] B. Kvamme, T. Kuznetsova, and K. Schmidt, “Experimental measurements and numerical modelling of interfacial tension in water-methane systems,” 2006.
- [47] S. Mirzaeifard, P. Servio, and A. D. Rey, “Multiscale Modeling and Simulation of Water and Methane Hydrate Crystal Interface,” *Cryst. Growth Des.*, vol. 19, no. 9, pp. 5142–5151, Sep. 2019, doi: 10.1021/acs.cgd.9b00578.
- [48] S. Mirzaeifard, P. Servio, and A. D. Rey, “Molecular dynamics characterization of the water-methane, ethane, and propane gas mixture interfaces,” *Chem. Eng. Sci.*, Feb. 2019, doi: 10.1016/j.ces.2019.01.051.
- [49] S. Mirzaeifard, P. Servio, and A. D. Rey, “Molecular Dynamics Characterization of Temperature and Pressure Effects on the Water-Methane Interface,” *Colloid Interface Sci. Commun.*, vol. 24, pp. 75–81, May 2018, doi: 10.1016/j.colcom.2018.04.004.
- [50] S. Mirzaeifard, P. Servio, and A. D. Rey, “Characterization of nucleation of methane hydrate crystals: Interfacial theory and molecular simulation,” *J. Colloid Interface Sci.*, vol. 557, pp. 556–567, Dec. 2019, doi: 10.1016/j.jcis.2019.09.056.
- [51] William F. Waite, “Thermal Properties of Methane Gas Hydrates: U.S. Geological Survey Fact Sheet 2007-3041,” 2007.
- [52] G. D. Holder, G. Corbin, and K. D. Papadopoulos, “Thermodynamic and Molecular Properties of Gas Hydrates from Mixtures Containing Methane, Argon, and Krypton,” *Ind. Eng. Chem. Fundam.*, vol. 19, no. 3, pp. 282–286, Aug. 1980, doi: 10.1021/i160075a008.
- [53] D. HUANG, S. FAN, D. LIANG, and Z. FENG, “Gas Hydrate Formation and Its Thermal Conductivity Measurement,” *Chin. J. Geophys.*, vol. 48, Sep. 2005, doi: 10.1002/cjg2.765.
- [54] H. Ghafari and H. Mohammadi-Manesh, “The thermal properties of binary structure sI clathrate hydrate from molecular dynamics simulation,” *Mol. Simul.*, vol. 45, no. 8, pp. 614–622, May 2019, doi: 10.1080/08927022.2019.1572142.
- [55] Y. P. Handa, “Compositions, enthalpies of dissociation, and heat capacities in the range 85 to 270 K for clathrate hydrates of methane, ethane, and propane, and enthalpy of dissociation of isobutane hydrate, as determined by a heat-flow calorimeter,” *J. Chem. Thermodyn.*, vol. 18, no. 10, pp. 915–921, Oct. 1986, doi: 10.1016/0021-9614(86)90149-7.

- [56] R. Nakagawa, A. Hachikubo, and H. Shoji, “Dissociation and specific heats of gas hydrate under submarine and sublacustrine environments,” in *Proceedings of the 6th International Conference on Gas Hydrates*, Vancouver, B.C., 2008, doi: 10.14288/1.0041144.
- [57] F. L. Ning, K. Glavatskiy, Z. Ji, S. Kjelstrup, and T. J. H. Vlugt, “Compressibility, thermal expansion coefficient and heat capacity of CH₄ and CO₂ hydrate mixtures using molecular dynamics simulations,” *Phys. Chem. Chem. Phys.*, vol. 17, no. 4, pp. 2869–2883, Dec. 2014, doi: 10.1039/C4CP04212C.
- [58] P. Rogl, R. Podloucky, and W. Wolf, “DFT Calculations: A Powerful Tool for Materials Design,” *J. Phase Equilibria Diffus.*, vol. 35, no. 3, pp. 221–222, Jun. 2014, doi: 10.1007/s11669-014-0309-7.
- [59] David S. Scholl and Janice A. Steckel, *Density Functional Theory: A Practical Introduction*. John Wiley & Sons, Inc., 2009.
- [60] David S. Scholl and Janice A. Steckel, “Density Functional Theory - From Wave Functions to Electron Density,” in *Density Functional Theory: A Practical Introduction*, John Wiley & Sons, Inc., 2009, p. 11.
- [61] Georg Kresse, Martijn Marsman, and Jurgen Furthmuller, *VASP the Guide*. Vienna: Computational Materials Physics, Faculty of Physics, Universitat Wien, 2016.
- [62] N. Crawford, F. Furche, and K. Burke, “Which functional should I choose?,” *Burke Res. Group*, Jan. 2009.
- [63] J. Sun, A. Ruzsinszky, and J. P. Perdew, “Strongly Constrained and Appropriately Normed Semilocal Density Functional,” *Phys. Rev. Lett.*, vol. 115, no. 3, p. 036402, Jul. 2015, doi: 10.1103/PhysRevLett.115.036402.
- [64] J. Sun *et al.*, “Accurate first-principles structures and energies of diversely bonded systems from an efficient density functional,” *Nat. Chem.*, vol. 8, no. 9, pp. 831–836, Sep. 2016, doi: 10.1038/nchem.2535.
- [65] R. Singh and M. K. Harbola, “A study of accurate exchange-correlation functionals through adiabatic connection,” *J. Chem. Phys.*, vol. 147, no. 14, p. 144105, Oct. 2017, doi: 10.1063/1.4995698.
- [66] M. Dion, H. Rydberg, E. Schröder, D. C. Langreth, and B. I. Lundqvist, “Van der Waals Density Functional for General Geometries,” *Phys. Rev. Lett.*, vol. 92, no. 24, p. 246401, Jun. 2004, doi: 10.1103/PhysRevLett.92.246401.
- [67] G. Román-Pérez and J. M. Soler, “Efficient Implementation of a van der Waals Density Functional: Application to Double-Wall Carbon Nanotubes,” *Phys. Rev. Lett.*, vol. 103, no. 9, p. 096102, Aug. 2009, doi: 10.1103/PhysRevLett.103.096102.
- [68] H. Peng, Z.-H. Yang, J. P. Perdew, and J. Sun, “Versatile van der Waals Density Functional Based on a Meta-Generalized Gradient Approximation,” *Phys. Rev. X*, vol. 6, no. 4, p. 041005, Oct. 2016, doi: 10.1103/PhysRevX.6.041005.

- [69] K. Lee, É. D. Murray, L. Kong, B. I. Lundqvist, and D. C. Langreth, “Higher-accuracy van der Waals density functional,” *Phys. Rev. B*, vol. 82, no. 8, p. 081101, Aug. 2010, doi: 10.1103/PhysRevB.82.081101.
- [70] F. Takeuchi, M. Hiratsuka, R. Ohmura, S. Alavi, A. K. Sum, and K. Yasuoka, “Water proton configurations in structures I, II, and H clathrate hydrate unit cells,” *J. Chem. Phys.*, vol. 138, no. 12, p. 124504, Mar. 2013, doi: 10.1063/1.4795499.
- [71] J. F. Stanton, “A refined estimate of the bond length of methane,” *Mol. Phys.*, vol. 97, no. 7, pp. 841–845, Oct. 1999, doi: 10.1080/00268979909482885.
- [72] C. Gutt, B. Asmussen, W. Press, M. R. Johnson, Y. P. Handa, and J. S. Tse, “The structure of deuterated methane-hydrate,” *J. Chem. Phys.*, vol. 113, no. 11, pp. 4713–4721, Sep. 2000, doi: 10.1063/1.1288789.
- [73] G. Herzberg, *Electronic Spectra and Electronic Structure of Polyatomic Molecules*. Krieger Publishing Company, 1991.
- [74] J. D. Bernal and R. H. Fowler, “A Theory of Water and Ionic Solution, with Particular Reference to Hydrogen and Hydroxyl Ions,” *J. Chem. Phys.*, vol. 1, no. 8, pp. 515–548, Aug. 1933, doi: 10.1063/1.1749327.
- [75] “IBRION - Vaspwiki.” Vienna Ab initio Simulation Package, 09-Apr-2019.
- [76] A. Togo and I. Tanaka, “First principles phonon calculations in materials science,” *Scr. Mater.*, vol. 108, pp. 1–5, Nov. 2015, doi: 10.1016/j.scriptamat.2015.07.021.
- [77] “EDDIFG - Vaspwiki.” Vienna Ab initio Simulation Package, 16-Apr-2019.
- [78] G. Kresse and J. Hafner, “Ab initio molecular dynamics for liquid metals,” *Phys. Rev. B*, vol. 47, no. 1, pp. 558–561, Jan. 1993, doi: 10.1103/PhysRevB.47.558.
- [79] G. Kresse and J. Hafner, “Ab initio molecular-dynamics simulation of the liquid-metal--amorphous-semiconductor transition in germanium,” *Phys. Rev. B*, vol. 49, no. 20, pp. 14251–14269, May 1994, doi: 10.1103/PhysRevB.49.14251.
- [80] G. Kresse and J. Furthmüller, “Efficiency of ab-initio total energy calculations for metals and semiconductors using a plane-wave basis set,” *Comput. Mater. Sci.*, vol. 6, no. 1, pp. 15–50, Jul. 1996, doi: 10.1016/0927-0256(96)00008-0.
- [81] G. Kresse and J. Furthmüller, “Efficient iterative schemes for ab initio total-energy calculations using a plane-wave basis set,” *Phys. Rev. B*, vol. 54, no. 16, pp. 11169–11186, Oct. 1996, doi: 10.1103/PhysRevB.54.11169.
- [82] M. Fishman, H. L. Zhuang, K. Mathew, W. Dirschka, and R. G. Hennig, “Accuracy of exchange-correlation functionals and effect of solvation on the surface energy of copper,” *Phys. Rev. B*, vol. 87, no. 24, p. 245402, Jun. 2013, doi: 10.1103/PhysRevB.87.245402.
- [83] “PREC - Vaspwiki.” Vienna Ab initio Simulation Package, 19-Apr-2019.
- [84] “ENCUT - Vaspwiki.” Vienna Ab initio Simulation Package, 07-Mar-2019.

- [85] P. E. Blöchl, "Projector augmented-wave method," *Phys. Rev. B*, vol. 50, no. 24, pp. 17953–17979, Dec. 1994, doi: 10.1103/PhysRevB.50.17953.
- [86] G. Kresse and D. Joubert, "From ultrasoft pseudopotentials to the projector augmented-wave method," *Phys. Rev. B*, vol. 59, no. 3, pp. 1758–1775, Jan. 1999, doi: 10.1103/PhysRevB.59.1758.
- [87] A. Togo, L. Chaput, I. Tanaka, and G. Hug, "First-principles phonon calculations of thermal expansion in Ti₃SiC₂, Ti₃AlC₂, and Ti₃GeC₂," *Phys. Rev. B*, vol. 81, no. 17, p. 174301, May 2010, doi: 10.1103/PhysRevB.81.174301.
- [88] "NCORE - Vaspwiki." Vienna Ab initio Simulation Package, 11-Mar-2019.
- [89] Peter Larsson, "Selecting the right number of cores for a VASP calculation - Peter Larsson," *National Supercomputer Centre at Linköping University*, 12-Jan-2015. [Online]. Available: <https://www.nsc.liu.se/~pla/blog/2015/01/12/vasp-how-many-cores/>. [Accessed: 27-Oct-2019].
- [90] "LPLANE - Vaspwiki." Vienna Ab initio Simulation Package, 11-Mar-2019.
- [91] "ISMEAR - Vaspwiki." Vienna Ab initio Simulation Package, 08-Oct-2019.
- [92] "SIGMA - Vaspwiki." Vienna Ab initio Simulation Package, 19-Apr-2019.
- [93] M. Sugisaki, H. Suga, and S. Seki, "Calorimetric Study of the Glassy State. IV. Heat Capacities of Glassy Water and Cubic Ice," *Bull. Chem. Soc. Jpn.*, vol. 41, no. 11, pp. 2591–2599, Nov. 1968, doi: 10.1246/bcsj.41.2591.
- [94] J. Costandy, V. K. Michalis, I. N. Tsimpanogiannis, A. K. Stubos, and I. G. Economou, "Molecular dynamics simulations of pure methane and carbon dioxide hydrates: lattice constants and derivative properties," *Mol. Phys.*, vol. 114, no. 18, pp. 2672–2687, Sep. 2016, doi: 10.1080/00268976.2016.1241442.
- [95] K. C. Hester, Z. Huo, A. L. Ballard, C. A. Koh, K. T. Miller, and E. D. Sloan, "Thermal Expansivity for sI and sII Clathrate Hydrates," *J. Phys. Chem. B*, vol. 111, no. 30, pp. 8830–8835, Aug. 2007, doi: 10.1021/jp0715880.
- [96] J. S. Tse, "Thermal expansion of structure-H clathrate hydrates," *J. Incl. Phenom. Mol. Recognit. Chem.*, vol. 8, no. 1, pp. 25–32, Jan. 1990, doi: 10.1007/BF01131285.
- [97] B. Yates, *Thermal expansion*. New York: Plenum Press, 1972.
- [98] K. Momma and F. Izumi, "VESTA3 for three-dimensional visualization of crystal, volumetric and morphology data," *J. Appl. Crystallogr.*, vol. 44, no. 6, pp. 1272–1276, Dec. 2011, doi: 10.1107/S0021889811038970.
- [99] F. Izquierdo-Ruiz, A. Otero-de-la-Roza, J. Contreras-Garcia, O. Prieto-Ballesteros, and J. M. Recio, "Effects of the CO₂ Guest Molecule on the sI Clathrate Hydrate Structure," *Materials*, vol. 9, no. 9, 2016.
- [100] L. Vočadlo, J. P. Poirer, and G. Price, "Grüneisen parameters and isothermal equations of state," *Am. Mineral.*, vol. 85, Feb. 2000, doi: 10.2138/am-2000-2-319.

[101] T. H. K. Barron, J. G. Collins, and G. K. White, “Thermal expansion of solids at low temperatures,” *Adv. Phys.*, vol. 29, no. 4, pp. 609–730, Aug. 1980, doi: 10.1080/00018738000101426.